JCI insight

A dual-reporter mouse for therapeutic discovery in Angelman syndrome

Hanna Vihma, Lucas M. James, Hannah C. Nourie, Audrey L. Smith, Siyuan Liang, Carlee A. Friar, Tasmai Vulli, Lei Xing, Dale O. Cowley, Alain C. Burette, Benjamin D. Philpot

JCI Insight. 2026. https://doi.org/10.1172/jci.insight.197028.

Resource and Technical Advance In-Press Preview **Genetics** **Neuroscience**

Angelman syndrome (AS) is a neurodevelopmental disorder caused by loss of the maternal *UBE3A* allele, the sole source of UBE3A in mature neurons due to epigenetic silencing of the paternal allele. Although emerging therapies are being developed to restore UBE3A expression by activating the dormant paternal *UBE3A* allele, existing mouse models for such preclinical studies have limited throughput and utility, creating bottlenecks for both in vitro therapeutic screening and in vivo characterization. To address this, we developed the *Ube3a*-INSG dual-reporter knock-in mouse, in which an IRES-Nanoluciferase-T2A-Sun1-sfGFP (INSG) cassette was inserted downstream of the endogenous Ube3a stop codon. The INSG model preserves UBE3A protein levels and function while enabling two complementary allele-specific readouts: Sun1-sfGFP and Nanoluciferase. We show that Sun1-sfGFP, a nuclear envelope-localized reporter, enables single-cell fluorescence analysis, whole-brain light-sheet imaging, and nuclear quantification by flow cytometry. Further, Nanoluciferase supports high-throughput luminescence assays for sensitive pharmacological profiling in cultured neurons and non-invasive in vivo bioluminescence imaging for pharmacodynamic assessment. By combining scalable screening, cellular analysis, and real-time in vivo monitoring in a single model, the *Ube3a*-INSG dual-reporter mouse provides a powerful platform to accelerate therapeutic development centered on UBE3A.

A dual-reporter mouse for therapeutic discovery in Angelman syndrome

Hanna Vihma[1], Lucas M. James[1], Hannah C. Nourie[1], Audrey L. Smith[1], Siyuan Liang[1], Carlee A. Friar[1], Tasmai Vulli[1], Lei Xing[1], Dale O. Cowley[2], Alain C. Burette[1,#], and Benjamin D. Philpot[1,3,#]

[1]Department of Cell Biology & Physiology, Neuroscience Center, University of North Carolina at Chapel Hill, NC, USA

[2]Animal Models Core, University of North Carolina at Chapel Hill, NC, USA

[3]Carolina Institute for Developmental Disabilities, University of North Carolina at Chapel Hill, NC, USA

[#]Corresponding authors:

BDP: 7008C Mary Ellen Jones, 116 Manning Drive, Campus Box 7545, Chapel Hill, NC 27599, USA. Telephone: +1 919-966-0031, bphilpot@med.unc.edu

ACB: 7004 Mary Ellen Jones, 116 Manning Drive, Campus Box 7545, Chapel Hill, NC 27599, USA. Telephone: +1 919-966-0031, alain_burette@med.unc.edu

Conflict of Interest Statement: DOC is employed by, has equity ownership in, and serves on the board of directors of TransViragen, the company contracted by UNC-Chapel Hill to manage its Animal Models Core Facility. BDP is a consultant for Astellas Gene Therapies.

Abstract

Angelman syndrome (AS) is a neurodevelopmental disorder caused by loss of the maternal *UBE3A* allele, the sole source of UBE3A in mature neurons due to epigenetic silencing of the paternal allele. Although emerging therapies are being developed to restore UBE3A expression by activating the dormant paternal *UBE3A* allele, existing mouse models for such preclinical studies have limited throughput and utility, creating bottlenecks for both *in vitro* therapeutic screening and *in vivo* characterization. To address this, we developed the *Ube3a*-INSG dual-reporter knock-in mouse, in which an IRES-Nanoluciferase-T2A-Sun1-sfGFP (INSG) cassette was inserted downstream of the endogenous *Ube3a* stop codon. The INSG model preserves UBE3A protein levels and function while enabling two complementary allele-specific readouts: Sun1-sfGFP and Nanoluciferase. We show that Sun1-sfGFP, a nuclear envelope-localized reporter, enables single-cell fluorescence analysis, whole-brain light-sheet imaging, and nuclear quantification by flow cytometry. Further, Nanoluciferase supports high-throughput luminescence assays for sensitive pharmacological profiling in cultured neurons and non-invasive *in vivo* bioluminescence imaging for pharmacodynamic assessment. By combining scalable screening, cellular analysis, and real-time *in vivo* monitoring in a single model, the *Ube3a*-INSG dual-reporter mouse provides a powerful platform to accelerate therapeutic development centered on UBE3A.

Introduction

Angelman syndrome (AS) is a rare neurodevelopmental disorder affecting approximately half a million individuals worldwide (1). Individuals with AS can have a normal lifespan, yet they face profound and lifelong challenges including severe motor dysfunction, intellectual disability, and an absence of speech, with epilepsy also commonly observed (2). These challenges create significant economic and social burdens for families and healthcare systems (3). AS is caused by disruption of the maternally inherited allele of the ubiquitin protein ligase E3A (*UBE3A*) gene (4–6). Both maternal and paternal copies of *UBE3A* are expressed in most cell types. However, in mature neurons, the paternal allele is epigenetically silenced by a long non-coding antisense transcript (*UBE3A-ATS*), leaving only the maternal allele to produce UBE3A (7).

Current standard of care practices for AS are limited to symptom management, with treatments such as antiepileptic drugs and behavioral therapies (8). Efforts to develop effective therapies have focused on restoring UBE3A protein levels in neurons. In particular, the unique parent-of-origin imprinting of *UBE3A* has prompted therapeutic strategies aimed at reactivating the dormant paternal allele. Several approaches have been developed to target *UBE3A-ATS* and restore UBE3A expression, including small molecules (9, 10), antisense oligonucleotides (ASOs) (11–15), artificial transcription factors (16), and CRISPR-based strategies including gene editing, transcriptional interference by dCas9, and RNA targeting with Cas13 (17–20). Among these, ASO therapies have advanced the furthest, with multiple candidates currently undergoing clinical evaluation (ClinicalTrials.gov: NCT06617429, NCT06914609, NCT04428281).

The YFP-tagged UBE3A fusion knock-in reporter mouse (RRID:IMSR_JAX:017765) has enabled allele-specific visualization of UBE3A expression and has served as a valuable screening platform for unsilencing compounds (9, 10, 21, 22). However, this model has notable

limitations: the YFP signal typically requires immunostaining for reliable detection, making quantitative analyses labor-intensive and lower throughput. In addition, UBE3A-YFP exhibits diffuse nuclear and cytoplasmic localization, which complicates single-cell quantification in densely packed tissues.

To address these limitations, we developed the *Ube3a*-INSG dual-reporter knock-in mouse model for sensitive, quantitative monitoring of UBE3A expression from either parental allele at single-cell resolution. The INSG allele encodes two reporters. Nanoluciferase (Nluc) enables high-throughput luminescence-based quantification and non-invasive *in vivo* bioluminescence imaging. Sun1-sfGFP, a nuclear envelope-anchored superfolder GFP (sfGFP) reporter, supports cellular-level quantitative immunofluorescence and flow cytometry. This dual-reporter design allows applications spanning high-throughput *in vitro* screening to high-resolution, whole-brain evaluation of biodistribution and pharmacodynamic effects *in vivo*. Here, we demonstrate the utility of this system in accelerating therapeutic development efforts centered on UBE3A.

Results

Generation of the *Ube3a*-INSG reporter mice

To generate the *Ube3a*-INSG reporter mouse line, we used CRISPR/Cas9-mediated genome editing to insert a 3566 bp reporter cassette immediately downstream of the *Ube3a* stop codon located in exon 13 (Figure 1A). The INSG reporter cassette includes an internal ribosomal entry site (IRES), a NanoLuciferase (Nluc) coding sequence, a T2A self-cleaving peptide from the *Thosea asigna* virus, and a Sun1-sfGFP fusion gene. The sfGFP is fused to an N-terminally truncated mouse (*Mus musculus*) Sun1 sequence, which directs the fusion protein to the nuclear envelope (23). The two reporters encoded by the INSG allele provide complementary strategies for monitoring *Ube3a* expression.

Due to epigenetic silencing of the paternal *Ube3a* allele, mice with the INSG transgene inherited paternally (patINSG) show minimal reporter expression in the brain at postnatal day 30 (P30), an age by which paternal *Ube3a* is silenced in neurons (Figure 1B) (22). Further, regions undergoing active neurogenesis – the subgranular zone of the dentate gyrus and the subventricular zone – along with areas where postnatal neurogenesis has recently ceased, such as the olfactory bulb and cerebellum, display sfGFP expression, consistent with their maturation status. In contrast, maternal inheritance of the INSG transgene (matINSG) leads to strong co-expression of endogenous UBE3A along with the Nluc and Sun1-sfGFP reporters (Figure 1C). Sagittal brain sections from matINSG mice show widespread GFP labeling that closely matches UBE3A expression, with the highest signals in the cerebrum (including cortex, hippocampus, basal ganglia, and olfactory bulb) and cerebellum, and the lowest in the brainstem (Figure 1B).

INSG insertion preserves UBE3A protein levels and function

Previous studies have shown that adding YFP or other protein linkers to the C-terminus of UBE3A can interfere with its expression or enzymatic activity, as reported for the *Ube3a*-YFP mouse model (24–26). In contrast, the INSG design avoids direct modification of the UBE3A protein. Instead, Nluc and Sun1-sfGFP are translated as independent polypeptides from the same transcript, rather than as fusion proteins. To assess whether inserting the INSG cassette downstream of *Ube3a* affects endogenous expression, we quantified *Ube3a* mRNA levels using primer sets located in exon 1 and within exons 4–5, 7–8, 11–12, and 12–13 (Figure 2A). These assays showed a progressive decrease in transcript abundance toward the 3′ end of the gene. Similar, but less pronounced, reductions were observed in patINSG and patYFP mice compared to wild-type (WT) mice (Supplementary Figure 1, A and B, respectively), suggesting that insertion into the 3′ UTR may influence transcript stability or processing. Despite these mRNA changes, western blot analysis showed that UBE3A protein levels were unchanged across genotypes (Figure 2, B-C), indicating that the insertion of the INSG cassette does not measurably impair UBE3A protein expression in either matINSG or patINSG mice.

To confirm whether inserting the INSG reporter cassette into the 3’ UTR of *Ube3a* affects UBE3A protein function, we performed anatomical and behavioral analyses in *Ube3a*-INSG mice (Figure 3). Since excessive adult weight gain and microcephaly are well-documented phenotypes in *Ube3a* maternal deletion AS mouse models (27–29), we evaluated body and brain weights at P90. MatINSG mice had body and brain weights similar to those of their WT littermates (Figures 3, A and B, respectively), indicating that the insertion of the INSG cassette does not disrupt overall growth or neurodevelopment. We then assessed whether the INSG insertion changes neurological function by testing matINSG mice for behavioral deficits commonly observed in AS models (30). Consistent with preserved UBE3A protein levels and function, matINSG mice showed no significant differences from WT littermates in locomotor

activity (open field distance, Figure 3C), motor coordination (accelerating rotarod, Figure 3D), or species-typical behaviors (marble burying, Figure 3E, and nest building, Figure 3F).

The maintained UBE3A protein levels and lack of anatomical and behavioral deficits compared to WT mice strongly support that inserting the INSG cassette does not compromise the functional integrity of UBE3A expressed from the INSG allele.

Sun1-sfGFP enables quantitative cellular analysis of UBE3A imprinting and paternal allele reactivation

Next, we examined how reliably Sun1-sfGFP reports UBE3A expression. We compared GFP and UBE3A immunolabeling patterns in matINSG and patINSG brains at P30. Our focus was on the hippocampus, where strong GFP labeling in the pyramidal cell layer of matINSG mice was substantially diminished in patINSG mice (Figures 4, A and B, respectively). The GFP signal remained high in the subgranular zone of the dentate gyrus, at the border between the granule cell layer and the hilus (arrows in Figure 4B), consistent with known paternal *Ube3a* expression in newly formed neurons (22).

Higher-resolution imaging of the CA1 hippocampal field revealed distinct Sun1-GFP labeling patterns dependent on reporter parent-of-origin (Figure 4, C-D). In matINSG brains, DAPI counterstaining showed intense GFP signal localized to the nuclear envelope of both pyramidal neurons and scattered smaller cells (Figure 4C). In contrast, the patINSG brain exhibited markedly reduced GFP staining confined to the nuclear membrane of a few smaller cells, presumed to be glial cells, with pyramidal neurons largely devoid of signal (Figure 4D). We used stimulated emission depletion (STED) microscopy to further validate the nuclear membrane localization of the GFP signal. Double-labelling for GFP and lamin B1, a canonical nuclear

envelope marker (31), revealed that GFP staining was interspersed with lamin B1 (Figure 4E). This pattern confirmed the expected nuclear envelope localization of the Sun1-sfGFP fusion protein (32).

We then directly compared the INSG model with the *Ube3a*-YFP reporter line by performing a side-by-side comparison of matINSG and matYFP brains at P13, using both native fluorescence and immunodetection (Figure 5). The Sun1-sfGFP reporter produced markedly superior signal resolution, even without signal enhancement (Figure 5A), yielding a sharp, ring-like pattern at the nuclear envelope that offered clear definition (Figure 5). In contrast, native YFP fluorescence was barely detectable in brain tissue (Figure 5A). Following antibody enhancement, the cytoplasmic YFP signal in *Ube3a*-YFP mice improved but appeared diffuse and poorly resolved in dense brain tissue, making cellular quantification more difficult (Figure 5B). These findings highlight the advantages of the INSG model for high-resolution imaging and accurate, cell-specific quantification of allele-specific UBE3A expression.

To highlight this utility, we performed quantitative analyses of UBE3A in the densely packed hippocampus. To identify the strongly labeled cells within the subgranular zone (SGZ) of the dentate gyrus, we carried out triple immunolabeling for GFP, UBE3A, and the microtubule-associated protein doublecortin (DCX) (Figure 6). In the adult dentate gyrus, DCX is expressed almost exclusively in developing neurons, serving as a reliable marker of neurogenesis (33). We observed that most SGZ cells with high GFP intensity co-expressed both DCX and UBE3A (Figure 6), consistent with these being immature neurons that biallelically express *Ube3a*. We then compared the mean GFP and UBE3A fluorescence intensities between DCX-positive SGZ cells and neurons in the surrounding granule cell layer (GCL) (Figure 6, E-F). In patINSG mice, GFP intensity was significantly higher in the SGZ than in the GCL, whereas in matINSG mice, strong GFP signals were present throughout the GCL. These findings support that paternal *Ube3a* expression is developmentally regulated and persists longer in immature neurons, as

shown by sustained reporter expression in DCX-positive cells. Although earlier studies have reported paternal *Ube3a* expression in immature neurons (22, 34), to our knowledge, this is the first quantitative *in vivo* analysis of this developmental pattern.

To validate that the cellular GFP reporter accurately reflects endogenous UBE3A, we examined expression in specific cell types following quintuple immunolabeling for GFP, UBE3A, and markers for astrocytes (SOX9), neurons (NeuN), and nuclei (DAPI) in the hippocampal CA1 field (Figure 7). In matINSG mice, robust GFP and UBE3A labeling was observed in both astrocytes (NeuN-negative/SOX9-positive) and mature neurons (NeuN-positive/SOX9-negative) (Figure 7, B and C, respectively). Analysis of 1,572 neurons showed high GFP expression ($\bar{x}$ = 0.452 ± 0.108; mean ± SD) with a strong linear correlation to UBE3A levels (Pearson r=0.559, Spearman ρ=0.549, p<0.0001). Astrocytes, which express UBE3A from both alleles, displayed more moderate GFP expression (n=2,306, $\bar{x}$ = 0.253 ± 0.075; mean ± SD) with a significant correlation to UBE3A (r=0.382, ρ=0.442, p<0.0001). In patINSG mice, neurons exhibited markedly reduced GFP labeling (n=2,059, $\bar{x}$ = 0.078 ± 0.053; mean ± SD), with only a few exceptions, while UBE3A labeling remained consistent ($\bar{x}$ = 0.354 ± 0.183; mean ± SD) (Figure 7C). Conversely, astrocytes continued to display strong labeling for both UBE3A and GFP, with the strongest correlation between the two (n=2,222, r=0.602, ρ=0.607, p<0.0001) (Figure 7B). These findings confirm biallelic *Ube3a* expression in glial cells, consistent with prior studies (22, 35, 21, 36), and extend these observations by providing a quantitative, cell-type-specific *in vivo* readout using a genetically encoded reporter.

Next, we tested the ability of Sun1-sfGFP to report *in vivo* reactivation of paternal *Ube3a* using (*S*)-PHA533533, a small molecule previously shown to unsilence paternal *Ube3a* after peripheral administration via a currently unidentified mechanism (10, 37). P11 patINSG mice received a single 2 mg/kg dose of (*S*)-PHA533533, while saline-treated matINSG and patINSG mice served as positive and negative controls, respectively (Figure 8). Analysis of Sun1-GFP

expression at P13, 48 hours post-treatment, in sagittal brain sections showed baseline GFP expression in patINSG brains compared to widespread signals in matINSG controls (Figure 8, A-B). In contrast, patINSG mice treated with (*S*)-PHA533533 showed visible partial reactivation of the GFP reporter across the brain (Figure 8C). Confocal imaging suggested that this reactivation happened within neuronal populations. This was especially in regions where neurons are readily distinguished by their size, shape, and location, including in superficial neocortical layers 1-2/3 (Figure 8, D-F), the pyramidal cell layer in the hippocampal CA1 field (Figure 8, G-I), and the dentate gyrus granule cell layer (Figure 8, J-L). This specific partial reactivation of paternal *Ube3a* by (*S*)-PHA533533 was further confirmed by co-staining with NeuN and SOX9 (Figure 8, M-N). Assessment of GFP intensity in nuclei across all three layers of the hippocampal CA1 region showed that SOX9-positive astrocytes maintained consistent GFP levels (Figure 8M) with no significant differences between matINSG and patINSG mice, regardless of treatment. These findings are consistent with biallelic *Ube3a* expression in glial cells, as previously reported in mice and non-human primates (21, 22, 35, 36), as well as (*S*)-PHA533533 not affecting *Ube3a* expression in biallelically expressing cell types (10). In contrast, we observed a significant difference in GFP intensity between saline-treated matINSG and patINSG mice in NeuN-positive neurons, reflecting paternal allele silencing (Figure 8N). Treatment of patINSG mice with 2 mg/kg (*S*)-PHA533533 increased GFP levels in NeuN-positive neurons, indicating partial reactivation of the paternal *Ube3a* allele (Figure 8N).

These data demonstrate that Sun1-sfGFP functions as a highly reliable, allele-specific reporter of UBE3A expression at regional and cellular levels. It accurately reflects *Ube3a* imprinting biology in the *Ube3a*-INSG mouse *in vivo* and sensitively reports pharmacologically-induced expression changes, demonstrating its ability to assess the pharmacodynamics of unsilencing approaches. The strict confinement of GFP signal to the nuclear envelope facilitates quantitative single-cell analysis in complex tissues.

INSG reporter enables whole-brain imaging of UBE3A expression

Assessing brain-wide UBE3A distribution is crucial for evaluating the efficacy of therapeutics aimed at reactivating paternal *Ube3a* expression. However, direct immunodetection of endogenous UBE3A in tissue-cleared whole brains proved challenging in our hands. Thus, we explored whether Sun1-GFP could overcome this problem by testing if the Sun1-sfGFP reporter could enable visualization of UBE3A-expressing nuclei in the intact brain using LSFM (Figure 9). We used the iDISCO clearing protocol with GFP immunolabeling in P30 INSG brains (38). The Sun1-sfGFP reporter provided robust and comprehensive labeling throughout the entire brain, overcoming the limitations of direct UBE3A detection (Figure 9). MatINSG brains exhibited widespread GFP signal faithfully reproducing known UBE3A expression patterns (Figure 9, A-C), while patINSG brains exhibited markedly reduced GFP signal. However, residual GFP labeling in patINSG brains was confined to regions of known persistent UBE3A expression, such as neurogenic zones including the rostral migratory stream, which is difficult to assess thoroughly in individual sections, and the dentate gyrus (Figure 9, B and D, respectively). High-resolution imaging in neocortical regions confirmed that Sun1-sfGFP enables visualization of individual nuclei throughout the brain volume, with its characteristic nuclear envelope localization providing single-cell resolution (Figure 9, E-F).

Dual Nluc and Sun1-GFP reporters enable high-throughput screening and flow cytometry analysis of allele-specific *Ube3a* expression

Previous screening efforts to identify compounds that unsilence paternal *Ube3a* relied on labor-intensive and costly high-content imaging workflows spanning multiple days (9, 10). The *Ube3a*-INSG reporter mouse was designed to enable robust, high-throughput *in vitro* screening via quantitative luminescence assays, made possible by the integrated Nluc reporter. To test this capability, we compared pharmacological profiles of the *Ube3a* unsilencer (*S*)-PHA533533 in primary neurons derived from patINSG mice using two complementary readouts: Nluc luminescence and ICC-based Sun1-sfGFP analysis (Figure 10, A-D). Efficacy measurements (half-maximal effective concentration; EC_{50}) derived from Nluc luminescence, mean GFP fluorescence, and the percentage of GFP-positive neurons were nearly identical, with overlapping 95% confidence intervals (Figure 10, A and C). Similarly, toxicity assessments (half-maximal cytotoxic concentration; CC_{50}) based on Nluc readout or by direct neuronal cell counting closely aligned (Figure 10, B and D). As expected, dose-response curves were highly similar across methods (Figure 10, C-D). Statistical comparisons further suggested no differences in potency and toxicity estimates between methods (Figure 10E), with small-to-medium Cohen's d effect sizes, a standardized measure of difference between two means that accounts for variability in the data (39). Importantly, the EC_{50} values derived from the INSG model closely matched those previously obtained using ICC in *Ube3a*-YFP neurons (10), despite the difference in detection method and reporter. Additionally, we sought to validate our Nluc system using another recently reported unsilencer, octanoic acid, a medium-chain fatty acid recently reported to improve behavioral phenotypes in AS mice (40). However, we observed no increase in Nluc signal in patINSG neurons following treatment with octanoic acid (Supplementary Figure 2A), whereas our positive control, (*S*)-PHA533533, robustly unsilenced paternal *Ube3a* in the same assay (Supplementary Figure 2B). To confirm this lack of unsilencing was not due to difference in reporter model, we dosed patYFP neurons with octanoic acid, but were again unable to detect the previously reported unsilencing of paternal *Ube3a* (Supplementary Figure 2C). Together, these results demonstrate that the Nluc-based

assay provides pharmacological data comparable to ICC for screening paternal *Ube3a* unsilencing small molecules, while offering substantially higher throughput.

To further evaluate the utility of the INSG system, we tested whether the Sun1-GFP reporter, which is anchored to the outer nuclear membrane, could be used for flow-cytometry-based analysis. Nuclei isolated from WT, matINSG, and patINSG neurons treated with 1 μM (*S*)-PHA533533 or DMSO for 72 hours were stained with DAPI and analyzed for GFP fluorescence (Figure 11, A-B). As expected, nuclei from matINSG cultures showed strong GFP fluorescence compared to WT controls. Fluorescence distributions from WT and matINSG samples were then used to set gating criteria for patINSG nuclei, which, under DMSO treatment, were largely GFP-negative. In contrast, (*S*)-PHA533533 treatment of patINSG neurons resulted in a clear increase in GFP-positive nuclei, approaching levels seen in untreated matINSG cultures (Figure 11, A-B). To directly compare performance with the *Ube3a*-YFP model, we performed the same assay using nuclei isolated from patYFP neurons. In this model, (*S*)-PHA533533 induced a barely detectable shift in fluorescence intensity (Figure 11, C-D), underscoring the limitations of the diffuse YFP signal for nuclear-sorting-based analyses. Together, these results demonstrate that Sun1-GFP provides a robust, allele-specific nuclear signal suitable for flow cytometric detection and sorting, underscoring a key advantage of the *Ube3a*-INSG reporter over the *Ube3a*-YFP model.

In addition to small-molecule reactivation, we assessed whether the INSG model could report antisense oligonucleotide (ASO)-mediated unsilencing of paternal *Ube3a* (Figure 12). To this end, we tested a previously validated ASO (ASO RTR26183) targeting *Ube3a-ATS* (13). Treatment of patINSG neurons with this ASO resulted in a dose-dependent increase in Nluc signal (Figure 12A), indicating paternal *Ube3a* unsilencing. This unsilencing was independently confirmed by RT-qPCR, which showed decreased *Ube3a-ATS* RNA together with increased

sfGFP mRNA levels (Figure 12, B-C, respectively). These results indicate that INSG reporter fidelity is preserved across distinct assay modalities.

To evaluate the utility of the *Ube3a*-INSG model beyond paternal unsilencing, we applied it to screen therapeutic candidates aimed at downregulating *Ube3a*. Dup15q syndrome is a neurodevelopmental disorder caused by maternal duplication or triplication of the 15q11.2-q13.1 region, which includes multiple genes, including *UBE3A* (41). Because maternally inherited duplications lead to more severe phenotypes than paternal duplications (42–44), UBE3A overexpression specifically in neurons is thought to be a major contributor to Dup15q syndrome (45–48). Accordingly, reducing UBE3A levels represents a promising therapeutic strategy. To this end, we screened six *Ube3a*-targeting ASOs in matINSG neurons. ASO treatment resulted in dose-dependent reductions in Nluc signal (Figure 12, D-E). Importantly, E_{MAX} values from the luciferase assay correlate with UBE3A protein knockdown, as measured by western blot, in WT neurons (Figure 12, F-G), validating the reporter as a proxy for endogenous protein levels. Together, these results highlight the value of the Nluc reporter for efficiently screening therapeutic compounds and ASOs in primary neuron cultures to identify drug/ASO candidates for both AS and Dup15q syndromes.

Nanoluciferase reporter enables *in vivo* bioluminescence imaging

Finally, we assessed whether the Nanoluciferase reporter allows *in vivo* bioluminescence imaging (BLI) in the INSG system. BLI offers a highly sensitive, non-invasive, and non-terminal method for pharmacodynamic profiling, making it well-suited for preclinical therapeutic studies. To evaluate this, 12-13-week-old adult female matINSG, patINSG, and WT littermates were injected with the fluorofurimazine substrate and imaged using an IVIS Spectrum system (Figure 13). Consistent with known UBE3A expression in peripheral tissues such as skin, we observed

strong Nluc bioluminescent signal from the paws, ears, nose, and tail of matINSG and patINSG mice, whereas WT mice showed no detectable signal (Figure 13A). These regions are naturally free of black fur in C57BL/6J mice, which enhances detection and underscores why albino/nude strains are commonly used for *in vivo* BLI (49).

To assess cranial signals, presumably reflecting reporter expression in the brain and overlaying tissues, we chemically removed scalp hair and repeated imaging one week later. As expected, signal from the tail and paws persisted, but importantly, bioluminescence from the scalp region became detectable in both matINSG and patINSG mice (Figure 13B). Although patINSG mice showed a robust cranial signal likely arising from non-neuronal sources and complicated by skin UBE3A expression, quantitative analysis revealed a clear increase in cranial signal intensity in matINSG mice, with approximately 50% higher signal compared to patINSG animals (Figure 13C). These results demonstrate that the INSG model enables *in vivo* BLI for non-invasive, quantitative assessment of paternal *Ube3a* unsilencing, as reflected by higher signals in matINSG compared to patINSG mice.

Discussion

We developed the *Ube3a*-INSG mouse model to accelerate preclinical development of therapeutics for AS. *Ube3a*-INSG integrates two complementary reporters: Nluc and Sun1-sfGFP. Nluc, which enables high-throughput, quantitative measurement of UBE3A expression and non-invasive bioluminescence imaging *in vivo*. Sun1-sfGFP, a nuclear envelope-localized GFP fusion facilitates flow cytometry and single-cell monitoring of UBE3A expression throughout the brain. This dual-reporter design introduces new capabilities that streamline therapeutic development and provides flexibility to use the same model across the entire preclinical pipeline – from rapid *in vitro* compound screening to detailed *in vivo* assessment of biodistribution and pharmacodynamic effects.

Because paternal *Ube3a* silencing is neuron-specific, unsilencing must be evaluated in post-mitotic neuronal systems, historically limiting the scalability of screening. To date, only ~5,100 small molecules have been screened across two published studies using high-content assays to identify paternal *Ube3a* unsilencers (9, 10). The *Ube3a*-INSG model enables far more scalable and rapid luciferase-based screening in primary neurons, supporting additional small molecule screening efforts. We demonstrated this screening capability by successfully replicating the pharmacological profile of (*S*)-PHA533533, a known *Ube3a* unsilencer, using the INSG model (10). Our luciferase assay yielded comparable potency and toxicity data to those from ICC-based detection in the *Ube3a*-YFP model, but at a significantly reduced time, cost, and technical complexity. Furthermore, we demonstrated the broad utility of the Nluc reporter by dose-dependent increases in luciferase signal in patINSG neurons following treatment with a *UBE3A-ATS*-targeting ASO, validating the model for high-throughput screening of both small molecules and ASO-based *Ube3a* unsilencers.

Beyond identifying unsilencers, the Nluc readout in matINSG neurons enables screening of compounds that reduce UBE3A levels, an application directly relevant to Dup15q syndrome. In Dup15q, maternal duplications or triplications of the 15q11.2-q13.1 region, where *UBE3A* resides, lead to its overexpression which contributes to core symptoms such as ASD, intellectual disability, and epilepsy (41). *Drosophila melanogaster* Dup15q models, in which overexpression of UBE3A homolog Dube3a induces spontaneous and pharmacoresistant seizures, have provided valuable insights into glial contributions to hyperexcitability and enabled high-throughput identification of seizure-suppressing compounds (50–53). However, no current preclinical mouse model offers comparable throughput for large-scale screens of UBE3A-lowering agents. Therefore, the *Ube3a*-INSG reporter and *Drosophila* seizure models are highly complementary, as UBE3A-lowering candidates identified using the INSG platform can subsequently be evaluated in seizure models to assess their functional impact. Thus, the Nluc-based readout enables scalable screening for UBE3A-lowering compounds in matINSG neurons and *Ube3a* unsilencers in patINSG neurons, supporting therapeutic discovery in both AS and Dup15q syndrome.

The Nluc reporter in the INSG model also supports non-invasive *in vivo* bioluminescence imaging. Systemic fluorofurimazine administration produced high cranial luminescence in matINSG mice, with lower levels observed in patINSG cranial areas. This approach could enable longitudinal assessment of UBE3A reporter activity in the same animals, providing a practical tool for tracking pharmacodynamic responses over time. Such repeated-measures designs enhance statistical power and allow evaluation of drug onset, duration, and efficacy without the need for serial tissue collection.

The strategic localization of Sun1-sfGFP to the nuclear envelope enables three key capabilities not achievable with prior models: allele-specific nuclear quantification of UBE3A in individual cells by IHC and flow cytometry, and whole-brain cellular profiling using LSFM. The sharp, ring-

like signal of Sun1-sfGFP provides clear resolution of individual cells for microscopy. This unambiguous morphology is amenable to automated segmentation pipelines such as InstantSeg, facilitating quantification of UBE3A expression at single-cell resolution (54). When combined with cell-type-specific markers, this system allows precise analysis within defined cellular populations, which we demonstrated in the CA1 hippocampal field. Such unsupervised, high-resolution quantification is impractical with the diffuse signal of UBE3A-YFP or UBE3A immunolabeling, especially in densely packed brain regions (22). Consistent with this, the INSG model is fully compatible with flow cytometry. We observed a clear increase in GFP-positive nuclei following (*S*)-PHA533533 treatment of patINSG neurons, validating Sun1-sfGFP as a robust allele-specific reporter for detecting UBE3A expression at the cellular level. This capability enables powerful downstream applications, including nuclear sorting for genetic and transcriptional interrogation of *Ube3a* unsilencing.

Sun1-sfGFP also enables whole-brain imaging with LSFM, which we used to visualize UBE3A expression across intact brains at cellular resolution. This is particularly valuable for AS therapeutic development, where treatment efficacy depends not only on restoring UBE3A levels but also on achieving a widespread and uniform distribution of interventions. Conventional IHC-based methods to evaluate therapeutic coverage are labor-intensive and spatially limited. In contrast, LSFM supports rapid, brain-wide imaging of cleared tissues at single-cell resolution. When combined with computational toolkits like MIRACL and ClearMap, this approach enables automated alignment to brain atlases and region-specific quantification, including cellular-level analysis in regions with low to moderate cell density, such as the neocortex (55, 56). These capabilities allow precise mapping of therapeutic distribution, identification of under-targeted areas, and evaluation of dose-dependent effects, providing a scalable and robust framework for optimizing delivery strategies. As such, Sun1-sfGFP combined with LSFM and advanced image

analysis substantially improves the precision and efficiency of *in vivo* assessment in preclinical AS studies.

While the *Ube3a*-INSG model presents clear advantages over historical reporter models, some limitations should be noted. Though UBE3A protein levels appear unaffected, the insertion of the reporter cassette into the *Ube3a* 3′ UTR results in reduced transcript levels in both matINSG and patINSG brains. This suggests potential effects on transcript stability or processing that warrant caution, particularly in studies focused on mRNA dynamics. Although biochemical and histological assessments indicate no major abnormalities, it is impossible to fully exclude subtle molecular or physiological effects caused by the knock-in construct. Therefore, we conducted anatomical and behavioral assessments, which are sensitive to UBE3A loss- and gain-of-function effects (27, 30, 57). The absence of abnormalities provides strong *in vivo* evidence that UBE3A protein function is preserved in the INSG model. Future detailed molecular characterizations of transcript dynamics would be valuable for a comprehensive understanding of the potential impacts of the reporter insertion. Additionally, the two reporters (Nluc and Sun1-sfGFP) differ in expression kinetics and stability from endogenous UBE3A, which may cause temporal mismatches when detecting rapid or transient changes, particularly relevant for short-term pharmacological studies requiring precise timing.

In summary, the *Ube3a*-INSG mouse model offers a comprehensive and versatile tool for advancing therapeutic development for AS and Dup15q syndrome. Its dual-reporter design enables high-throughput compound screening, single-cell quantification, and whole-brain evaluation. These integrated capabilities position the *Ube3a*-INSG model as a powerful platform to accelerate preclinical research and support the discovery of safe and effective therapies for AS and other UBE3A-related disorders.

Methods

Sex as a biological variable

Both male and female animals were included. Behavioral outcomes were comparable across sexes, and data were pooled, whereas body weight was analyzed by sex. For primary neuron cultures, cortices from embryos of both sexes were pooled within litters.

CRISPR/Cas9 reagents

Guide RNAs (gRNAs) targeting the mouse *Ube3a* 12th intron and 3′UTR (60-80 bp from the stop codon) were designed using Benchling (RRID:SCR_013955). To minimize off-target effects, high-fidelity eSpCas9 was used together with tRNA-gRNA fusion RNAs to avoid heterologous 5′ nucleotide additions that impair Cas9 activity. gRNAs were cloned into a T7-tRNA-gRNA construct (UNC Animal Models Core), transcribed *in vitro* using the HiScribe T7 High Yield RNA Synthesis Kit (E2040S, New England BioLabs), and purified via RNeasy spin columns (74104, Qiagen) in microinjection buffer (5 mM Tris-HCl pH 7.5, 0.1 mM EDTA). gRNA activity was validated by electroporating each gRNA with recombinant eSpCas9 into mouse embryonic fibroblasts (UNC Animal Models Core). Cells were harvested ~72 hrs post-electroporation, and target site were PCR-amplified, sequenced, and analyzed using the Inference of CRISPR Edits (ICE, Synthego Inc., RRID:SCR_024508). The selected gRNAs were Ube3a-5g62B (5′-ATG TAT ATC GAA GTC TAC CT-3′) and Ube3a-3g41T (5′-ATA TAA GAG GGA TAA TTT GA-3′). A donor plasmid containing: (i) 1002-bp 5′ homology arm (upstream of the Ube3a-5g62B PAM, with the PAM mutated from AGG to AGC); (ii) 669-bp wild-type sequence spanning from the mutated PAM in intron 12 to the *Ube3a* stop codon in exon 13; (iii) 3566-bp INSG reporter cassette containing IRES, Nluc, 2A self-cleaving peptide from *Thosea asigna* virus capsid protein (T2A), Sun1 nuclear envelope localization domain

fused to the N-terminus of superfolder GFP (Addgene #160141), and FRT site; (iv) 63-bp wild-type sequence from the start of the *Ube3a* 3′UTR to the Ube3a-3g41T PAM (with the PAM mutated from TGG to TTG); and (v) 997-bp 3′ homology arm immediately downstream of the mutated PAM. The donor vector was prepared using a High Speed Maxiprep (12662, Qiagen), eluted in microinjection buffer, and dialyzed using a 0.05 µM mixed cellulose ester membrane (VMWP02500, Millipore) against a 20-fold excess of microinjection buffer for at least 1 hour.

Embryo microinjection

C57BL/6J zygotes were microinjected with a mixture containing 400 nM eSpCas9 protein, 33 ng/µl of each gRNA, and 20 ng/µl donor plasmid in microinjection buffer (5 mM Tris-HCl pH 7.5, 0.1 mM EDTA) and then implanted into pseudopregnant B6D2F1 females. Founder pups were screened by PCR for correct INSG cassette integration at the 5′ and 3′ junctions. One female founder carrying the intended insertion, but also exhibiting vector backbone sequences, was crossed with a Flp-transgenic male B6J-Tg(CAG-Flpo) (UNC Animal Models Core) to eliminate tandem integrations. One F1 male with a correct single-copy insertion and lacking the Flp transgene was bred to wild-type C57BL/6J females to establish the line.

Mice

Knock-in mice expressing yellow fluorescent protein (YFP) fused to the C-terminus of *Ube3a* were originally generated in the laboratory of A. Beaudet (21)(RRID:IMSR_JAX:017765). Both *Ube3a*-YFP and *Ube3a*-INSG mice were maintained on a coisogenic C57BL/6J background under standard housing conditions with *ad libitum* access to food and water. Paternal or maternal inheritance of the *Ube3a* reporter allele was generated by crossing wild-type females

with reporter males or wild-type males with reporter females, respectively. Genotyping primers are listed in Supplementary Table 1.

Western blot analysis

Tissues were snap-frozen in liquid nitrogen and stored at -80°C until lysis. Primary mouse neurons were washed once with PBS before lysis. Cells and tissues were lysed in ice-cold RIPA lysis buffer (50 mM Tris–HCl pH 8.0, 150 mM NaCl, 1% NP-40, 0.5% sodium deoxycholate, 0.5% SDS) supplemented with protease inhibitor cocktail (P8340, Millipore Sigma). Cultured cells were lysed by repeatedly pipetting with a 1 mL pipette tip in lysis buffer, while tissues were homogenized using a Tissue Tearor (Model 985-370). Lysates were incubated on ice for 10 min, sonicated 3 times for 5 sec, and centrifuged at maximum speed for 10 min at 4°C to remove insoluble cell debris. Protein concentrations were measured using the Pierce BCA protein assay kit (23227, Thermo Scientific). A total of 30 µg of each sample was separated on 7.5% Mini-PROTEAN TGX gel (4561024, Bio-Rad) and transferred at 90 mA for 90 min onto 0.45 µm Immobilon-FL PVDF membrane (05317, MilliporeSigma) in ice-cold transfer buffer (25 mM Tris-base, 192 mM glycine, and 20% MeOH). Membranes were blocked in Intercept® (PBS) Blocking Buffer (927-70001, LI-COR Biosciences) for 1 hour and incubated with primary antibodies (Supplementary Table 2) overnight at 4°C. After washing three times with PBS/0.5% Tween-20, membranes were incubated with HRP-conjugated secondary antibodies for 1 hour at RT. Chemiluminescence signals were detected using Clarity Western ECL substrate (1705061, Bio-Rad), imaged on an Amersham Imager 680 (GE Healthcare), and quantified using ImageJ (RRID:SCR_003070).

RNA isolation and RT-qPCR

For tissue RNA extraction, half-brains from adult mice were snap-frozen immediately following dissection and stored at -80°C until processing. Tissues were lysed in RLT buffer (79216, Qiagen) with 1% β-mercaptoethanol, and total RNA was isolated using the RNeasy Mini kit (74104, Qiagen) according to the manufacturer's protocol. For cultured neurons, media were removed, cells were washed once with PBS, and RNA was isolated using TRIzol reagent (250 µL per well; 15596026, Thermo Fisher Scientific) following the manufacturer's protocol. cDNA was synthesized from 1 µg (tissue) or 250 ng (neurons) of total RNA using qScript cDNA Supermix (95048, Quantabio). RT-qPCR reactions were performed using 1/25th of the synthesized cDNA with PowerUp SYBR Green Master Mix (A25742, Applied Biosystems) and gene-specific primers (Supplementary Table 3) on a QuantStudio 5 Real-Time PCR system (Applied Biosystems) with melting curve analysis to confirm specificity. *Ube3a* primers were obtained from (58). Assays were performed in technical quadruplicates, averaged per sample, and normalized to *Eif4a2* using the comparative CT (ΔΔCT) method.

Tissue preparation for histology

Mice received intraperitoneal injections of Euthasol (a mixture of pentobarbital sodium and phenytoin sodium, 100 mg/kg, i.p., Virbac, ANADA #200-071) for deep anesthesia, followed by intracardiac perfusion with phosphate-buffered saline (PBS, 0.1 M, pH 7.3) and then with 4% freshly depolymerized paraformaldehyde in phosphate buffer (pH 7.4) for 10 minutes. Brains were extracted, post-fixed overnight at 4°C in the same fixative, and cryoprotected in 30% sucrose in PBS until saturated. For confocal and STED microscopy, brains were sectioned at 50 µm thickness using a sliding microtome and stored at -20°C in a cryopreservative solution (45% PBS, 30% ethylene glycol, 25% glycerol) until use.

Immunolabelling for confocal and STED microscopy

Free-floating sections were rinsed twice in PBS (5 minutes each), permeabilized in PBS containing 0.1% Triton-X-100 (PBS-T), and blocked for 30 min at room temperature in PBS-T containing 10% FBS. Sections were incubated overnight with primary antibodies (Supplementary Table 2), followed by PBS-T washes and overnight incubation with fluorophore-conjugated secondary antibodies. Sections were counterstained with DAPI (1 µg/mL; D1306, Invitrogen), washed, and mounted on gelatin-coated slides. Slides were air-dried and coverslipped using Vectashield Plus (H-1900, Vector Laboratories) for confocal microscopy or Abberior Mount Liquid (MM-2007, Abberior GmbH) for STED imaging. Images were acquired using a Leica STELLARIS 8 FALCON microscope and quantified using QuPath (RRID: SCR_018257, 59) and InstanSeg (https://github.com/instanseg, 54). InstanSeg uses a deep learning convolutional neural network to enable accurate segmentation of cellular and nuclear boundaries for single-cell quantification.

Immunolabelling for LSFM

Brain clearing and immunolabeling followed the iDISCO protocol (38). Briefly, brains were sequentially dehydrated in methanol/PBS (5-100%, 30 min per step), incubated overnight in 66% dichloromethane/33% methanol, washed twice in 100% methanol, and bleached in 5% H_2O_2 in methanol at 4°C for 24 hours. Tissues were rehydrated through a descending methanol series (100-10%, 30 min per step), washed twice in 0.2% Triton X-100/PBS for 1 hour, and permeabilized at 37°C for 48 hours (0.2% Triton X-100, 2% glycine, 20% DMSO in PBS). Tissues were blocked for 48 hours (0.2% Triton X-100, 1% BSA) and incubated with primary

antibodies (Supplementary Table 2) for 6 days in antibody solution (0.2% Tween-20, 40 mg/L heparin, 11% BSA, 5% DMSO in PBS). After washing (0.2% Tween-20, 40 mg/l heparin in PBS), samples were incubated with secondary antibodies for 6 days, followed by dehydration in methanol, dichloromethane treatment, and clearing in dibenzyl ether. Imaging was performed using Ultramicroscope II (LaVision BioTec) and visualized with Imaris (RRID:SCR_007370).

Behavioral assays

Behavioral testing began ~P70. Assays were administered in order of increasing stress, with 2-3 days between tests.

1) *Open field*: Locomotor activity in a novel environment was assessed for 30 minutes in an open field chamber (40 cm × 40 cm × 30 cm) contained inside sound-attenuating boxes with ceiling-mounted lights. Mice were video-recorded, and total distance traveled was quantified in 5-min bins using Ethovision XT 15.0 (Noldus; RRID:SCR_000441).
2) *Marble burying*: Mice were placed for 30 min in clean cages containing 3 L of corncob bedding (~5 cm deep; Andersons Lab, 1/8 in diameter, irradiated) with 20 black glass marbles (14 mm diameter) arranged in a 5 × 4 grid. Overhead images were acquired before and after testing, and the percentage of marble area obscured by bedding was quantified using ImageJ (RRID:SCR_003070, NIH).
3) *Rotarod*: Balance and motor coordination were assessed on an accelerating rotarod (Ugo Basile). Mice were tested from 4 to 40 rpm over 5 min. Three trials were conducted during the initial session and two additional trials 48 hours later, with 3-5 min intertrial intervals. Latency to fall or to three consecutive passive rotations was recorded.
4) *Nest building*: Mice were single-housed for 3 days before testing. Nesting material was replaced with 11 ± 1 g of compressed blot filter paper (1703966, Bio-Rad) cut into eight equal rectangles, and unused material was weighed daily for 5 days.

Drug and ASO preparation

(*S*)-PHA533533 was synthesized as previously described (37, 60, 61). Octanoic acid was purchased from Sigma-Aldrich (O3907, Lot. SHBL4414). For *in vitro* assays, all drugs were formulated in DMSO (0.1% final). For *in vivo* assays, (*S*)-PHA533533 was dissolved in 0.9% NaCl. All ASOs were synthesized by Integrated DNA Technologies (IDT) and diluted in PBS (Supplementary Table 4). The *Ube3a-ATS*-targeting ASO (named RTR26183), previously described (13), is a fully phosphorothioate-modified oligonucleotide composed of locked nucleic acid (LNA) and DNA bases, with 5-methylcytosine-modified LNA cytosines. The six *Ube3a*-targeting ASOs (ASO #1-6), described in patent WO2023239782A2, are 2′-MOE gapmers with a phosphorothioate backbone.

Mouse primary neuron cultures

Timed pregnant female mice (3 to 5 months old) were euthanized via cervical dislocation. Cortices from E15.5 embryos from both sexes were dissected in Leibovitz's L-15 Medium (11415064, ThermoFisher) and rinsed with HBSS (14025076, ThermoFisher). Cortices were then incubated for 30 min at 37°C in papain (1 vial diluted with 2.5 mL of HBSS; 88285, ThermoFisher) with DNase I (20 mg/mL; D4513, Sigma) in HBSS. To deactivate the papain, 1 mL of DMEM containing 10% FBS (TMS-013-B, Millipore Sigma), GlutaMax (35050-061, Invitrogen), and Antibiotic-Antimycotic (15240-062, Invitrogen) was added to the cortical tissue, followed by trituration. The cells were centrifuged for 2 min at 4600 × *g*, washed with HBSS, and resuspended in DMEM with 10% FBS, GlutaMax, and Antibiotic-Antimycotic. The cells were filtered through a 70-micron filter and incubated at 37°C for 15 min on a sterile tissue culture

plate to remove glial cells (similarly to 62). The supernatant was carefully collected, and cells were plated in Neurobasal Plus Medium (A3582901, ThermoFisher) containing B27 Plus (A3582801, ThermoFisher), GlutaMax (35050-061, Invitrogen), and Antibiotic-Antimycotic (15240-062, Invitrogen) onto poly-D-lysine coated black-walled 384-well plates at $2x10^4$ cells/well for dose-response assays, 24-well plate at $2.5x10^5$ cells/well for RT-qPCR assays, or 6-well plates at $1.5x10^6$ cells/well for flow cytometry. Cultured neurons were maintained by half-medium changes every 3-4 days using Neurobasal Plus, GlutaMax, B27 Plus, and 2.46 μg/mL 5-fluoro-2´-deoxyuridine (F0503, Sigma).

ICC, high-content imaging, and dose-response analysis in cultured neurons

The immunofluorescence protocol for high-content imaging was previously described (10). Neurons were treated at DIV7 with (*S*)-PHA533533 or 0.1% DMSO for 72 hours, washed with PBS, and fixed in 4% PFA for 10 min at room temperature. Cells were permeabilized with 1% Triton X-100 in PBS for 10 min and blocked for 30 min in PBS containing 5% NGS and 0.2% Triton X-100 (NGST). Neurons were incubated overnight at 4°C with primary antibodies in NGST (Supplementary Table 2), followed by incubation with secondary antibodies and DAPI (133 ng/mL; D1306, Invitrogen) for 60 min at room temperature. Images were acquired on a Nikon Ti2 Eclipse fluorescence microscope (Nikon Instruments) and analyzed using NIS-Elements software. Potency (EC_{50}) of paternal *Ube3a*-INSG unsilencing was determined using two complementary ICC-based metrics: (i) mean normalized GFP intensity in $DAPI^+/NeuN^+$ neurons relative to DMSO controls and (ii) the percentage of $GFP^+/DAPI^+/NeuN^+$ neurons, using a GFP threshold set to yield ~5% GFP^+ neurons in DMSO-treated wells. Cytotoxicity (CC_{50}) was assessed as the percentage of surviving $DAPI^+/NeuN^+$ neurons relative to DMSO controls. For E_{MAX} determination, only concentrations resulting in <10% reduction in neuronal survival were

included; the highest concentration within this non-toxic range defining the response plateau was designated as the maximal effect.

Luciferase assay and dose-response analysis

For the dose-response assay for (*S*)-PHA533533 (Figure 8, C-D) and *Ube3a*-targeting ASOs (Figure 8, I-J), neurons were treated at DIV7 for 72 hours. Cells were washed with PBS and lysed with 1x Passive Lysis Buffer (25 µl per well, E1941, Promega) for 15 min. NanoLuc activity was measured using coelenterazine H (301, NanoLight Technology), prepared as a 1 mM stock in ethanol and diluted to 20 µM in mQ, with luminescence recorded over a 1-second integration time on a CLARIOstar Plus (BMG Labtech) microplate reader with injector (10 µL substrate per well). Relative light units were normalized to DMSO-treated controls. EC_{50} values for patINSG unsilencing were determined using concentrations that produced increasing luminescence up to a plateau, whereas CC_{50} values were calculated from concentrations beyond the plateau where luminescence declined due to cell loss.

For dose-response assays of *Ube3a*-targeting ASO (Figure 8F) and octanoic acid together with (*S*)-PHA533533 (Supplementary Figure 2, A-B), neurons were treated at DIV7 for 72 hours. Cell viability was assessed using CellTiter-Fluor assay (G6080, Promega) in 25 µl of fresh media containing 20% of assay buffer and 25 µM of GF-AFC substrate per well, followed by luminescence measurement using the Nano-Glo Luciferase Assay System (N1110, Promega), according to the manufacturers' protocols. Fluorescence and luminescence were measured on a CLARIOstar Plus (BMG Labtech) microplate reader.

Isolation of nuclei and flow cytometry analysis

Neuronal cultures were maintained for 10 days in 6-well plates at 1.5 x10^6 neurons/well. Nuclei were isolated by lysing each well in 0.5 mL Nuclei PURE lysis buffer (NUC102, Sigma-Aldrich) supplemented with 0.5 µL 1 M DTT and 5 µL 10% Triton X-100. Lysates were collected, triturated, incubated on ice for 5 min, and centrifuged at 500 × g for 5 min. Pellets were resuspended in 250 µL cold DPBS containing 1% BSA (SP-5050-500, Vector Lab), mixed with 400 µL 2 M sucrose (S9308, Sigma-Aldrich), layered onto 250 µL 2 M sucrose, and centrifuged at 13,000 × g for 45 min to separate nuclei from debris. Nuclei were resuspended in 500 µL DPBS containing 1% BSA and 2 µg/mL DAPI (D1306, Invitrogen) (adapted from 63).

Flow cytometry was performed on a BD Melody cell sorter (Becton Dickinson) with a 100-µm nozzle. Ten thousand nuclei events were acquired per replicate. Nuclei were gated by DAPI fluorescence with violet laser, followed by FSC-A/SSC-A to select low-complexity events; GFP and YFP were excited with the blue laser. Data were analyzed using FlowJo v10.10 (RRID:SCR_008520, BD Bioscience).

***In vivo* bioluminescence imaging**

Female 12-13-week-old matINST, patINSG, and WT littermate mice were used for *in vivo* bioluminescence imaging. Mice were briefly anesthetized with 2.5% isoflurane and injection intraperitoneally with fluorofurimazine (FFz; 2 mg/kg; 50-313-4464, Selleck Chemical) dissolved in 10% DMSO, 40% PEG300 and 50% DPBS. After a 5-min recovery, mice were re-anesthetized for imaging, with anesthesia maintained at 1.5% isoflurane and the stage temperature set to 37°C. Images were acquired at 10 min post-FFz administration using an IVIS Spectrum system (Revvity Inc.) with the following settings: FOV D, focus 1.5 cm, binning 8,

f/stop 1, and 5-second exposure (no emission filter). One week later, the same animals were imaged under identical conditions following chemical hair removal over the skull using depilatory cream. Background signal was determined from WT mice, subtracted with clipping, and normalized to patINSG mice within each imaging session.

Statistics

All data analyses were conducted using GraphPad Prism 10.4.1 (RRID:SCR_002798), except for Figure 7, which was analyzed using OriginPro 2023b (OriginLab). All individual data values, statistical tests, sample sizes (N), and significance thresholds are provided in the Supporting Data Values file and referenced in the main text or figure legends. A P-value < 0.05 was considered statistically significant.

Study approval

All animal studies were conducted in accordance with NIH guidelines under an IACUC-approved protocol at the University of North Carolina School of Medicine.

Data availability

All data supporting the findings of this study are provided in the Supporting Data Values file. Full-resolution light-sheet microscopy datasets are available from the corresponding author upon reasonable request and can be shared via an external hard drive or institutional file transfer services. No custom code was generated for this study; all analyses were performed using commercially available software as described in the Methods.

Funding support

This work was supported in part by funding from the National Institutes of Health and is subject to the NIH Public Access Policy.

This work was supported by National Institute of Neurological Disorders and Stroke (NINDS) grants R01NS131615 and R01NS129914 (to B.D.P.) and by a grant from the Angelman Syndrome Foundation (to B.D.P.). Imaging and core facility access were supported in part by institutional and shared-resource grants, including the NIH Cancer Center Core Support Grant P30 CA016086 to the UNC Lineberger Comprehensive Cancer Center and NIH grant 1S10OD030300 (confocal microscopy), NIH grant P30 CA016086 and the North Carolina Biotech Center Institutional Support Grant 2016-IDG-1016 (light-sheet microscopy), and the NIH-NINDS Neuroscience Center Support Grant P30 NS045892 and the NIH-NICHD Intellectual and Developmental Disabilities Research Center Grant P50 HD103573 (high-content imaging). The UNC Animal Models Core Facility is supported in part by NIH grant P30 CA016086.

Author contributions

HV and DOC designed the *Ube3a*-INSG reporter mouse. ALS performed *in vivo* dosing. HV, ALS, HN, and SL established primary neuronal cultures. ALS and LMJ designed, conducted, and analyzed behavioral experiments. ALS and SL performed western blotting. LMJ and SL conducted RT-qPCR analysis. LMJ performed *in vitro* ASO assays. HCN performed flow cytometry experiments and analysis, as well as octanoic acid assays. CAF and ACB performed histology and microscopy. ACB performed quantitative analysis of *in vivo* fluorescence. TV assisted with colony management and perfusions. HV conducted *in vitro* ICC, high-content

analysis, and luciferase assays. LMJ and LX performed *in vivo* bioluminescence imaging and analysis. HV, LMJ, HCN, and ACB analyzed data and provided scientific supervision. HV, LMJ, ACB, and BDP oversaw the project. HV wrote the manuscript with input from all authors. BDP secured funding and provided intellectual guidance for the project. All authors reviewed, edited, and approved the final version of the manuscript.

Acknowledgments

We thank Anna Welton-Arndt (Department of Chemistry) and Jeffrey Aubé (Division of Chemical Biology and Medicinal Chemistry; Department of Chemistry) from UNC Chapel Hill for synthesizing (*S*)-PHA533533 used in this study.

References

1. Almeida JFM de, Tonazzini I, Daniele S. Molecular aspects of Angelman Syndrome: Defining the new path forward. *Biomol Biomed*. 2025;25(9):1928–1936.

2. Dagli A, Buiting K, Williams CA. Molecular and Clinical Aspects of Angelman Syndrome. *Mol Syndromol*. 2012;2(3–5):100–112.

3. Jarvis J, et al. The economic impact of caregiving for individuals with Angelman syndrome in the United States: results from a caregiver survey. *Orphanet J Rare Dis*. 2025;20:82.

4. Kishino T, Lalande M, Wagstaff J. UBE3A/E6-AP mutations cause Angelman syndrome. *Nat Genet*. 1997;15(1):70–73.

5. Matsuura T, et al. De novo truncating mutations in E6-AP ubiquitin-protein ligase gene (UBE3A) in Angelman syndrome. *Nat Genet*. 1997;15(1):74–77.

6. Cooper EM, et al. Biochemical analysis of Angelman syndrome-associated mutations in the E3 ubiquitin ligase E6-associated protein. *J Biol Chem*. 2004;279(39):41208–41217.

7. Vu TH, Hoffman AR. Imprinting of the Angelman syndrome gene, UBE3A , is restricted to brain. *Nat Genet*. 1997;17(1):12–13.

8. Keary CJ, McDougle CJ. Current and emerging treatment options for Angelman syndrome. *Expert Rev Neurother*. 2023;23(9):835–844.

9. Huang H-S, et al. Topoisomerase inhibitors unsilence the dormant allele of Ube3a in neurons. *Nature*. 2011;481(7380):185–189.

10. Vihma H, et al. Ube3a unsilencer for the potential treatment of Angelman syndrome. *Nat Commun*. 2024;15(1):5558.

11. Clarke MT, et al. Prenatal delivery of a therapeutic antisense oligonucleotide achieves broad biodistribution in the brain and ameliorates Angelman Syndrome phenotype in mice. *Mol Ther*. 2024;32(4):935–951.

12. Dindot SV, et al. An ASO therapy for Angelman syndrome that targets an evolutionarily conserved region at the start of the UBE3A-AS transcript. *Sci Transl Med*. 2023;15(688):eabf4077.

13. Jagasia R, et al. Angelman syndrome patient neuron screen identifies a potent and selective clinical ASO targeting UBE3A-ATS with long lasting effect in cynomolgus monkey. *Nucleic Acids Res*. 2025;53(16):gkaf851.

14. Meng L, et al. Towards a therapy for Angelman syndrome by targeting a long non-coding RNA. *Nature*. 2015;518(7539):409–412.

15. Milazzo C, et al. Antisense oligonucleotide treatment rescues UBE3A expression and multiple phenotypes of an Angelman syndrome mouse model. *JCI Insight*. 2021;6(15):145991.

16. O'Geen H, et al. Transcriptional reprogramming restores UBE3A brain-wide and rescues behavioral phenotypes in an Angelman syndrome mouse model. *Mol Ther*. 2023;31(4):1088–1105.

17. Rs S, et al. CRISPR/Cas9 directed to the Ube3a antisense transcript improves Angelman syndrome phenotype in mice. *J Clin Invest*. 2021;131(5).

18. Wolter JM, et al. Cas9 gene therapy for Angelman syndrome traps Ube3a-ATS long non-coding RNA. *Nature*. 2020;587(7833):281-284

19. Wolter JM, et al. AAV-dCas9 vector unsilences paternal Ube3a in neurons by impeding Ube3a-ATS transcription. *Commun Biol*. 2025;8(1):1332.

20. Li J, et al. A high-fidelity RNA-targeting Cas13 restores paternal Ube3a expression and improves motor functions in Angelman syndrome mice. *Mol Ther J Am Soc Gene Ther*. 2023;31(7):2286–2295.

21. Dindot SV, et al. The Angelman syndrome ubiquitin ligase localizes to the synapse and nucleus, and maternal deficiency results in abnormal dendritic spine morphology. *Hum Mol Genet*. 2008;17(1):111–118.

22. Judson MC, et al. Allelic specificity of Ube3a expression in the mouse brain during postnatal development. *J Comp Neurol*. 2014;522(8):1874–1896.

23. Lawler AJ, et al. Cell Type-Specific Oxidative Stress Genomic Signatures in the Globus Pallidus of Dopamine-Depleted Mice. *J Neurosci*. 2020;40(50):9772–9783.

24. Xing L, et al. A luminescence-based biosensor to measure endogenous UBE3A activity. *iScience*. 2025;28(11):113684.

25. Kelkar GR, et al. A human Angelman Syndrome class II pluripotent stem cell line with fluorescent paternal UBE3A reporter. *Front Cell Dev Biol*. 2025;13:1665693.

26. Filonova I, et al. Activity-dependent changes in MAPK activation in the Angelman Syndrome mouse model. *Learn Mem*. 2014;21(2):98–104.

27. Jiang YH, et al. Mutation of the Angelman ubiquitin ligase in mice causes increased cytoplasmic p53 and deficits of contextual learning and long-term potentiation. *Neuron*. 1998;21(4):799–811.

28. Judson MC, et al. Decreased Axon Caliber Underlies Loss of Fiber Tract Integrity, Disproportional Reductions in White Matter Volume, and Microcephaly in Angelman Syndrome Model Mice. *J Neurosci*. 2017;37(31):7347–7361.

29. Ozarkar SS, et al. Comparative profiling of white matter development in the human and mouse brain reveals volumetric deficits and delayed myelination in Angelman syndrome. *Mol Autism*. 2024;15(1):54.

30. Sonzogni M, et al. A behavioral test battery for mouse models of Angelman syndrome: a powerful tool for testing drugs and novel Ube3a mutants. *Mol Autism*. 2018;9:47.

31. Gruenbaum Y, Foisner R. Lamins: Nuclear Intermediate Filament Proteins with Fundamental Functions in Nuclear Mechanics and Genome Regulation. *Annu Rev Biochem*. 2015;84(1):131–164.

32. Mo A, et al. Epigenomic Signatures of Neuronal Diversity in the Mammalian Brain. *Neuron*. 2015;86(6):1369–1384.

33. Brown JP, et al. Transient expression of doublecortin during adult neurogenesis. *J Comp Neurol*. 2003;467(1):1–10.

34. Hillman PR, et al. Genomic imprinting does not reduce the dosage of UBE3A in neurons. *Epigenetics Chromatin*. 2017;10(1):1–14.

35. Yamasaki K, et al. Neurons but not glial cells show reciprocal imprinting of sense and antisense transcripts of Ube3a. *Hum Mol Genet*. 2003;12(8):837–847.

36. Gonzalez Ramirez C, et al. Regional and cellular organization of the autism-associated protein UBE3A/E6AP and its antisense transcript in the brain of the developing rhesus monkey. *Front Neuroanat*. 2024;18:1410791.

37. Pevarello P, et al. 3-Aminopyrazole Inhibitors of CDK2/Cyclin A as Antitumor Agents. 2. Lead Optimization. *J Med Chem*. 2005;48(8):2944–2956.

38. Renier N, et al. iDISCO: a simple, rapid method to immunolabel large tissue samples for volume imaging. *Cell*. 2014;159(4):896–910.

39. Cohen J. *Statistical Power Analysis for the Behavioral Sciences*. New York: Routledge; 2013.

40. Qu S, et al. Dietary Intake of Octanoic Acid Restores UBE3A Expression and Improves the Behavioral Phenotypes in a Mouse Model of Angelman Syndrome. *FASEB J Off Publ Fed Am Soc Exp Biol*. 2025;39(8):e70559.

41. LaSalle JM, Reiter LT, Chamberlain SJ. Epigenetic regulation of UBE3A and roles in human neurodevelopmental disorders. *Epigenomics*. 2015;7(7):1213–1228.

42. Eh C, et al. Autism or atypical autism in maternally but not paternally derived proximal 15q duplication. *Am J Hum Genet*. 1997;60(4):928–34.

43. Hogart A, et al. The comorbidity of autism with the genomic disorders of chromosome 15q11.2-q13. *Neurobiol Dis*. 2010;38(2):181–91.

44. Isles AR, et al. Parental Origin of Interstitial Duplications at 15q11.2-q13.3 in Schizophrenia and Neurodevelopmental Disorders. *PLoS Genet*. 2016;12(5):e1005993.

45. Punt AM, et al. Molecular and behavioral consequences of *Ube3a* gene overdosage in mice. *JCI Insight*. 2022;7(18):e158953.

46. Elamin M, et al. The role of UBE3A in the autism and epilepsy-related Dup15q syndrome using patient-derived, CRISPR-corrected neurons. *Stem Cell Rep*. 2023;18(4):884–898.

47. Copping NA, et al. Neuronal overexpression of Ube3a isoform 2 causes behavioral impairments and neuroanatomical pathology relevant to 15q11.2-q13.3 duplication syndrome. *Hum Mol Genet*. 2017;26(20):3995–4010.

48. Noor A, et al. 15q11.2 Duplication Encompassing Only the UBE3A Gene Is Associated with Developmental Delay and Neuropsychiatric Phenotypes. *Hum Mutat*. 2015;36(7):689–693.

49. Collaco AM, Geusz ME. Monitoring immediate-early gene expression through firefly luciferase imaging of HRS/J hairless mice. *BMC Physiol*. 2003;3:8.

50. Hope KA, LeDoux MS, Reiter LT. Glial overexpression of Dube3a causes seizures and synaptic impairments in Drosophila concomitant with down regulation of the Na+/K+ pump ATPα. *Neurobiol Dis*. 2017;108:238–248.

51. Roy B, et al. An Unbiased Drug Screen for Seizure Suppressors in Duplication 15q Syndrome Reveals 5-HT1A and Dopamine Pathway Activation as Potential Therapies. *Biol Psychiatry*. 2020;88(9):698–709.

52. Landaverde S, et al. Glial expression of Drosophila UBE3A causes spontaneous seizures that can be modulated by 5-HT signaling. *Neurobiol Dis*. 2024;200:106651.

53. Geier B, Roy B, Reiter LT. Small molecule ion channel agonist/antagonist screen reveals seizure suppression via glial Irk2 activation in a Drosophila model of Dup15q syndrome. *Neurobiol Dis*. 2025;208:106882.

54. Goldsborough T, et al. A novel channel invariant architecture for the segmentation of cells and nuclei in multiplexed images using InstanSeg [preprint]. https://doi.org/10.1101/2024.09.04.611150. Posted on bioRxiv September 8, 2024.

55. Goubran M, et al. Multimodal image registration and connectivity analysis for integration of connectomic data from microscopy to MRI. *Nat Commun*. 2019;10(1):5504.

56. Renier N, et al. Mapping of Brain Activity by Automated Volume Analysis of Immediate Early Genes. *Cell*. 2016;165(7):1789–1802.

57. Xing L, et al. Autism-linked UBE3A gain-of-function mutation causes interneuron and behavioral phenotypes when inherited maternally or paternally in mice. *Cell Rep*. 2023;42(7):112706.

58. Lee D, et al. Antisense oligonucleotide therapy rescues disturbed brain rhythms and sleep in juvenile and adult mouse models of Angelman syndrome. *eLife*. 2023;12:e81892.

59. Bankhead P, et al. QuPath: Open source software for digital pathology image analysis. *Sci Rep*. 2017;7(1):16878.

60. Nesi M, et al. A practical synthesis of the major 3-hydroxy-2-pyrrolidinone metabolite of a potent CDK2/cyclin A inhibitor. *Bioorg Med Chem Lett*. 2006;16(12):3205–3208.

61. Pevarello P, et al. 3-Aminopyrazole inhibitors of CDK2/cyclin A as antitumor agents. 1. Lead finding. *J Med Chem*. 2004;47(13):3367–3380.

62. Sahu MP, et al. Culturing primary neurons from rat hippocampus and cortex. *Neuronal Signal*. 2019;3(2):NS20180207.

63. Ayhan F, et al. Nuclei isolation from surgically resected human hippocampus. *STAR Protoc*. 2021;2(4):100844.

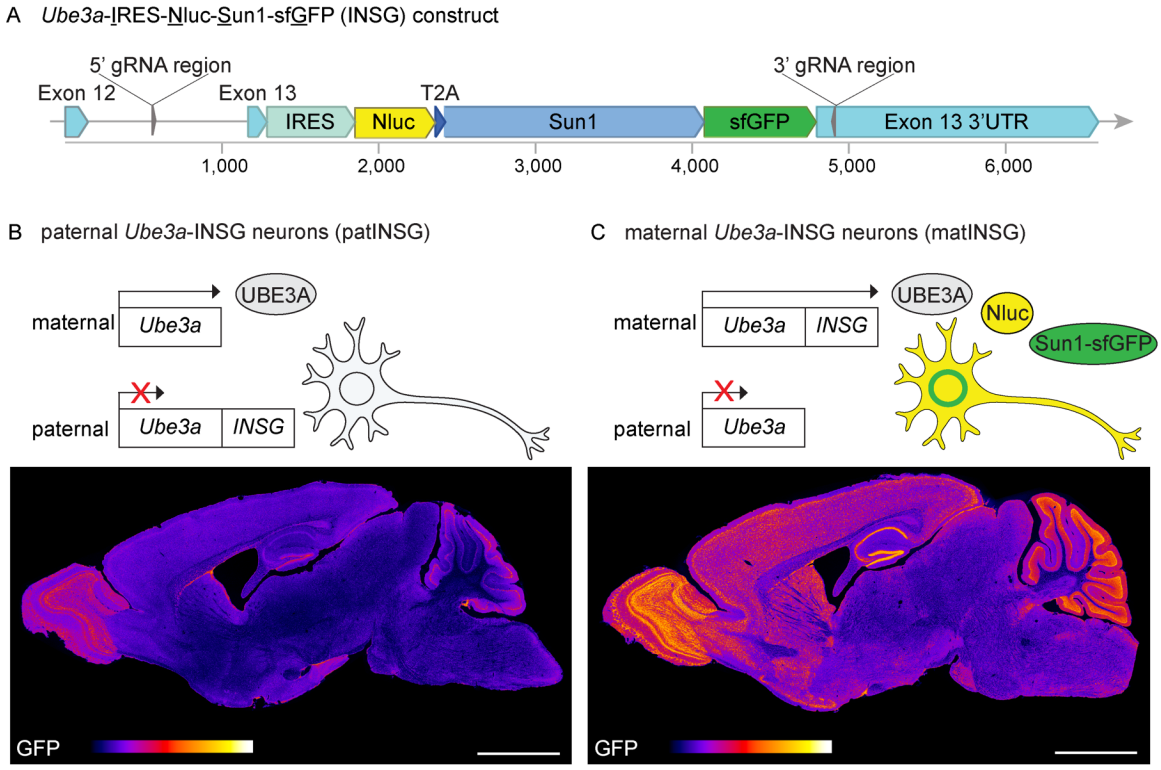

Figure 1. Generation and allele-specific expression of the *Ube3a-IRES-Nluc-Sun1-sfGFP* (*INSG*) reporter allele. (**A**) Schematic of the INSG construct and gRNAs used for pronuclear microinjection. The 3566 bp INSG reporter cassette was inserted downstream of the *Ube3a* stop codon in exon 13. It includes an internal ribosomal entry site (IRES), nanoluciferase coding sequence (Nluc), 2A self-cleaving peptide from *Thosea asigna* virus capsid protein (T2A), and Sun1 nuclear envelope localization domain (Sun1) fused to the N-terminus of superfolder GFP (sfGFP). The 5' and 3' guide RNA target site regions used for the homologous recombination are shown in *Ube3a* intron 12 and 3' UTR, respectively. (**B**) Schematic of the paternal allele expression of the *Ube3a*-INSG transgene (patINSG), where *Ube3a*-INSG is paternally inherited and silenced in neurons, resulting in maternal-only UBE3A expression in most mature neurons. The sagittal section from a postnatal day 30 (P30) patINSG brain shows low overall GFP signal, with some residual expression in the olfactory bulb, newborn neurons in the dentate gyrus, and cerebellar cortex. (**C**) Schematic of the maternal allele expression of the *Ube3a*-INSG transgene (matINSG), where *Ube3a*-INSG is maternally inherited, enabling expression of UBE3A, Nluc, and Sun1-sfGFP from the maternal allele. The corresponding sagittal section shows strong GFP labeling in the cerebrum and cerebellum, with lower signal in the brainstem. Scale bars: 2 mm. Fire gradient used for visualization.

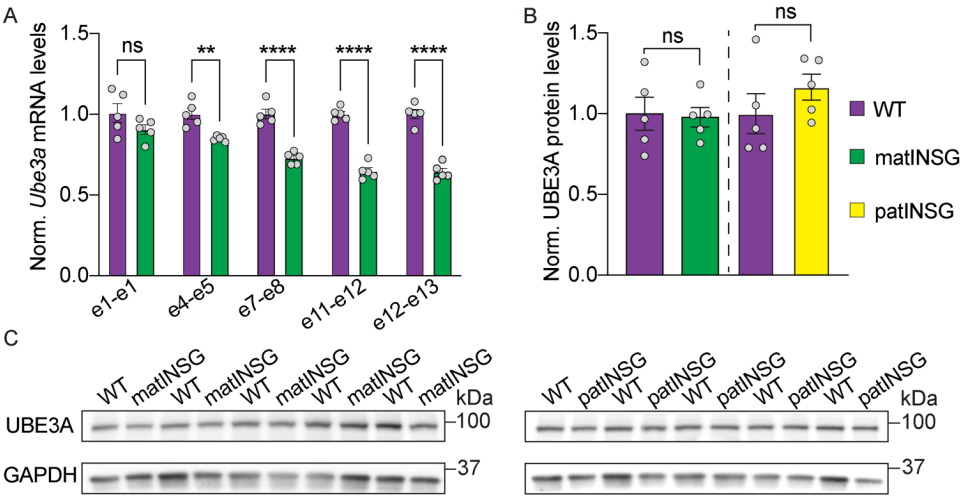

Figure 2. Insertion of INSG reporter cassette into the *Ube3a* 3' UTR preserves UBE3A protein levels. Brains from postnatal day 90 (P90) mice were split so that one hemisphere was used for RNA extraction and the opposite hemisphere for protein analysis. Data from both assays were normalized to WT littermate controls. (**A**) Quantification of *Ube3a* mRNA normalized to *Eif4a2* in WT and matINSG using primer sets targeting the indicated exons (two-way ANOVA with Bonferroni's *post hoc* test). (**B**) Quantification of UBE3A protein levels in WT, matINSG, and patINSG mice normalized to GAPDH (two-tailed t-test). (**C**) Representative western blots comparing WT vs. matINSG and WT vs. patINSG. Each data point represents an individual animal (N = 5 per genotype; all males), with data shown as means ± SEM. ns = non-significant, *P < 0.05, **P < 0.005, ****P < 0.0001. Detailed statistical comparisons are provided in the source data file. Norm., normalized; e, exon.

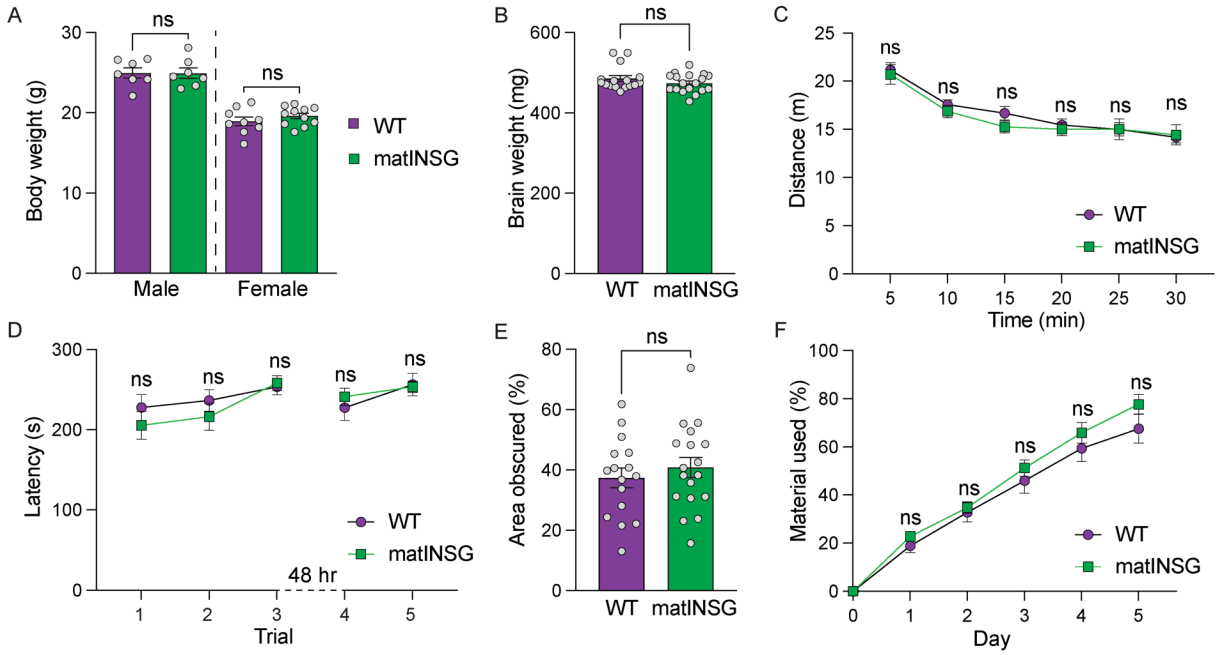

Figure 3. Insertion of INSG reporter cassette into the *Ube3a* 3' UTR preserves UBE3A protein function. (**A**) Body weight and (**B**) brain weight did not differ significantly between wild-type (WT) and matINSG mice (two-tailed t-test). (**C-F**) Behavioral phenotyping shows no significant differences between WT and matINSG mice in (**C**) distance traveled in the open field (two-way repeated-measures ANOVA, Bonferroni's *post hoc* test), (**D**) latency to fall on an accelerating rotarod (two-way repeated-measures ANOVA, Bonferroni's *post hoc* test), (**E**) percentage of marble area obscured by bedding in a 30-minute test session (two-tailed t-test), and (**F**) nesting material used over a 5-day nest-building assay (two-way repeated-measures ANOVA, Bonferroni's *post hoc* test). Body weight and brain weight were measured at postnatal day 90 (P90). Behavioral tests were conducted on the same cohort beginning around P70 (WT: N = 18 [7 males, 11 females]; matINSG: N = 16 [7 males, 9 females]), and performed in the order shown. Each data point represents an individual animal, with data shown as means ± SEM. ns = non-significant. Detailed statistical comparisons are provided in the source data file.

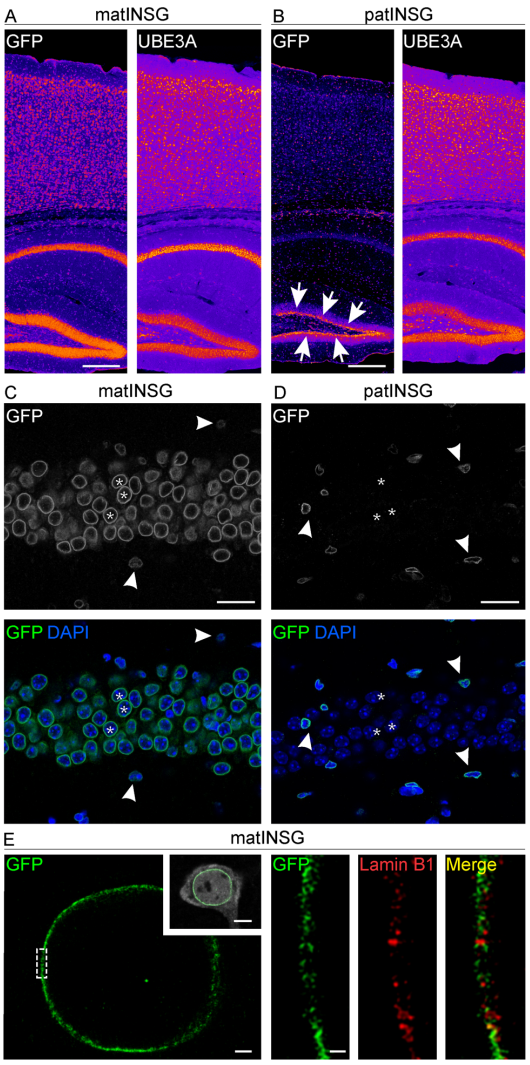

Figure 4. Validation of Sun1-sfGFP as an allele-specific, nuclear envelope-localized reporter of UBE3A expression. (**A-B**) Hippocampal and cortical regions in postnatal day 30 (P30) matINSG and patINSG mice. (**A**) In matINSG brain, GFP (left) and UBE3A (right) levels are closely matched. (**B**) In patINSG brain, GFP (left) is sparser than UBE3A (right), with a strong signal only in immature neurons of the dentate gyrus subgranular zone (arrows). Fire gradient used for visualization. (C–D) High magnification of the hippocampal CA1 region. (**C**) In matINSG, DAPI (blue, bottom) and GFP staining (gray, top; green, bottom) show expression in pyramidal neurons (asterisks) and smaller cells outside the layer (arrowheads). (**D**) In patINSG, only scattered small cells, presumably glia, are GFP-positive (gray, top; green, bottom) (arrowheads), while pyramidal neurons lack staining (asterisks). In both genotypes, GFP localizes to the nuclear membrane, consistent with Sun1 fusion. (E) STED microscopy of a matINSG neuron showing Sun1-sfGFP localization at the nuclear envelope. GFP from the boxed region (left) is shown at higher magnification to the right, alongside Lamin B1 and the merged image, confirming membrane localization. The insert in (**E**) shows an overview of the same cell stained for NeuN (gray) and GFP (green). Scale bars: 250 μm (A, B); 25 μm (C, D); 1 μm (E); 5 μm (insert in E); 200 nm (right panel in E).

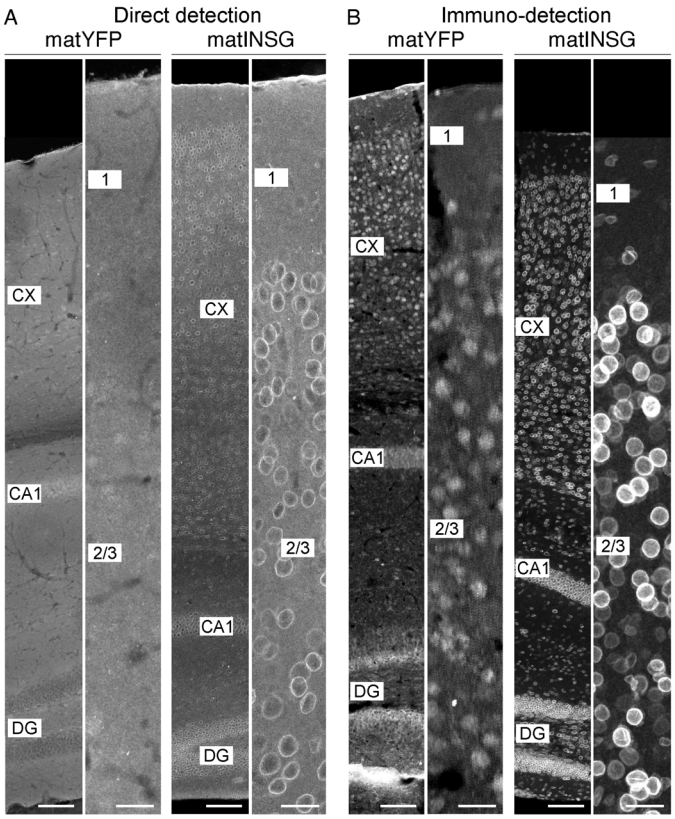

Figure 5. The matINSG Sun1-sfGFP reporter provides superior signal and cellular resolution compared to matYFP. (**A**) Direct fluorescence detection in matYFP and matINSG mice at postnatal day 13 (P13) showing the neocortex (CX) and hippocampal region (CA1 region and DG, dentate gyrus). No specific signal is readily visible in matYFP mice beyond background fluorescence, whereas matINSG mice exhibit a weak but clearly detectable nuclear-localized sfGFP signal. (**B**) Immunodetection using GFP antibody in matYFP and matINSG mice. The INSG reporter demonstrates superior cellular resolution with distinct nuclear labeling, while YFP shows more diffuse cytoplasmic staining. Higher magnification images of neocortex layer 1 to 3 (right panels in A and B) highlight individual cells and the improved signal-to-background ratio in matINSG mice. Scale bars: 25 µm (left micrographs); 100 µm (right micrographs).

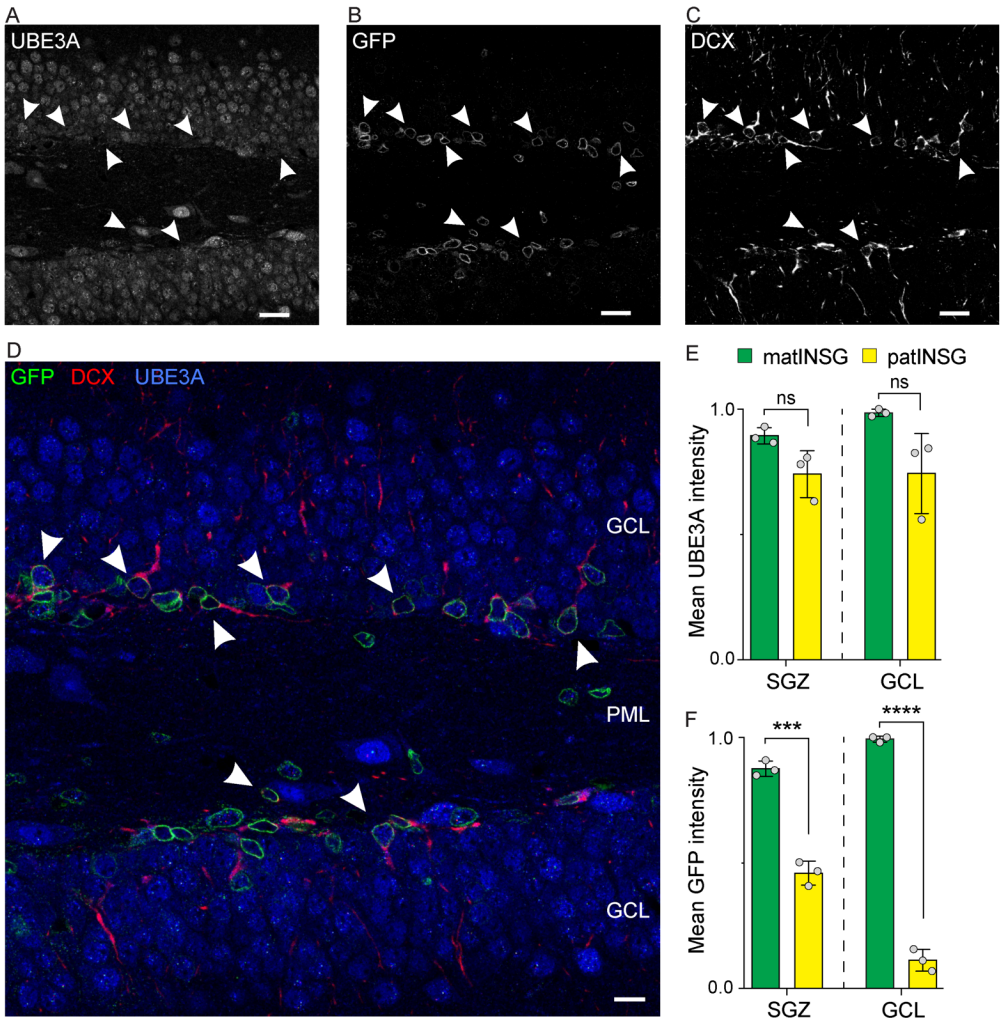

Figure 6. Sun1-sfGFP is expressed in immature neurons in the patINSG hippocampus. Triple immunofluorescence staining of the dentate gyrus in postnatal day 30 (P30) patINSG mice for (**A**) UBE3A, (**B**) Sun1-sfGFP (GFP), and (**C**) the immature neuron marker doublecortin (DCX). (**D**) The merged image highlights that, in contrast to the widespread detection of UBE3A, GFP expression is restricted chiefly to DCX-positive immature neurons (arrowheads) located in the subgranular zone. (**E**) Mean intensity of UBE3A and GFP in the subgranular zone (SGZ; defined by DCX staining) and in the granule cell layer (GCL) of the dentate gyrus in matINSG and patINSG mice (N = 3 animals per group). Data are presented as mean ± SEM. One-tailed unpaired t-test (ns = non-significant, ***P < 0.001, ****P < 0.0001). PML, polymorphic layer. Scale bar: 20 µm (A-C); 10µm (D).

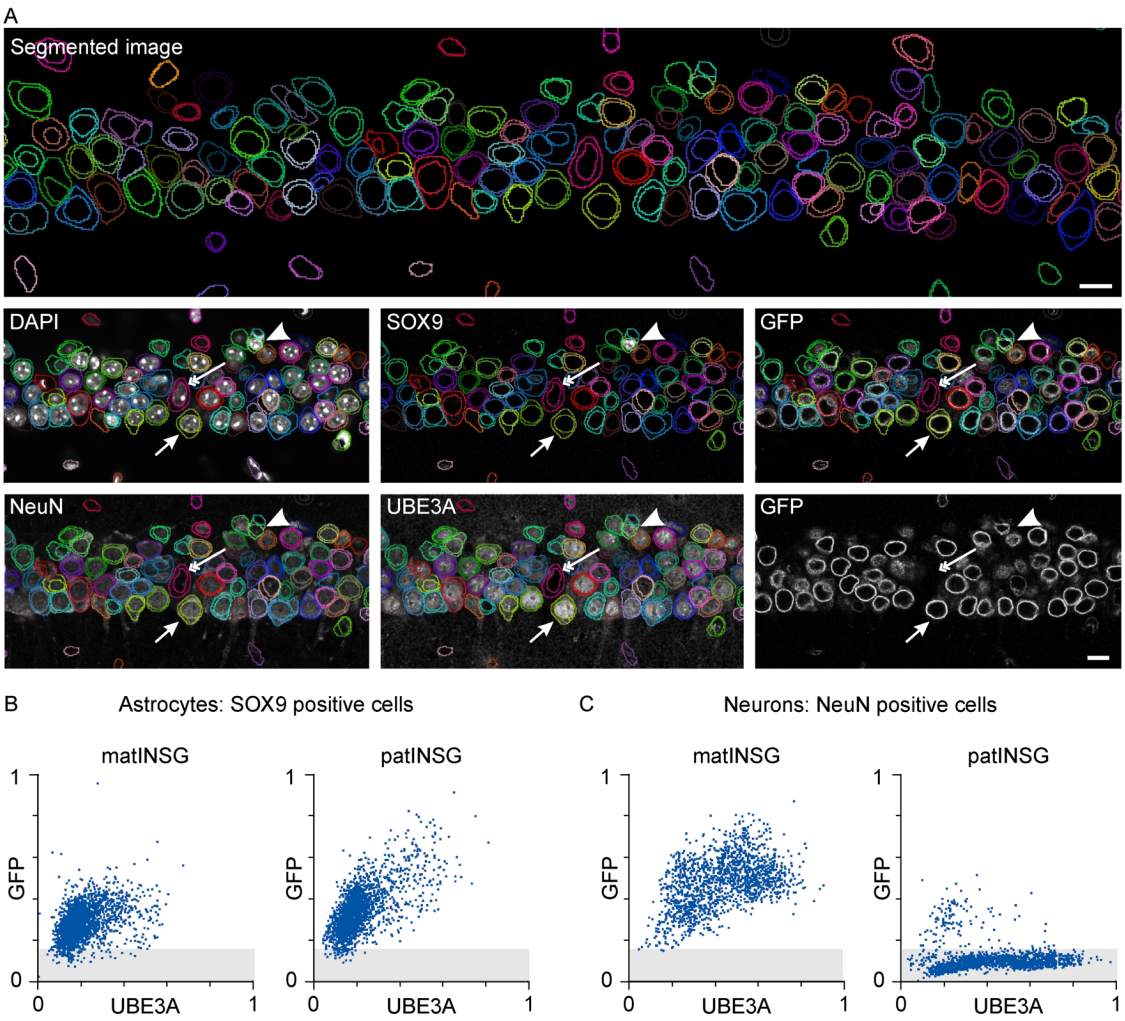

Figure 7. Relationship between UBE3A and Sun1-sfGFP labeling in individual cells in matINSG versus patINSG mice. (**A**) An illustration of the effectiveness of the deep learning algorithm used to quantify UBE3A and Sun1-sfGFP expression at single-cell resolution, even in densely packed areas like the hippocampal CA1 region. For easier visualization, each cell is outlined with a randomly assigned color to indicate both nuclear and cytoplasmic boundaries. Each of the six smaller panels overlays the cell segmentation results with one of the five input channels (DAPI, SOX9, GFP, NeuN, or UBE3A) used for segmentation, while the bottom right panel shows only the GFP channel without cell segmentations. The arrow points to a likely pyramidal neuron that expresses GFP, UBE3A, and the neuronal marker NeuN but not the astrocyte marker SOX9. The arrowhead indicates a small cell that is GFP-, UBE3A-, and SOX9-positive, but NeuN-negative. The double arrow identifies an outlier cell lacking all tested markers. (**B** and **C**) Scatter plots depicting the relationship between GFP and UBE3A fluorescence levels in individual cells within the hippocampal CA1 region at postnatal day 30 (P30). (**B**) In SOX9-positive astrocytes, GFP and UBE3A intensities strongly correlate in matINSG and patINSG mice. (**C**) In NeuN-positive neurons, there is a strong correlation between GFP and UBE3A intensities in matINSG mice but not patINSG mice, apart from a small subset of cells, as most neurons in patINSG mice display GFP levels at background levels. The grey shaded area marks the range of background GFP fluorescence observed in UBE3A-positive neurons from patINSG samples (panel C, right), which lack Sun1-sfGFP

expression. This reference range is shown across all plots to facilitate comparison across genotypes and cell types. Scale bars: 10 μm.

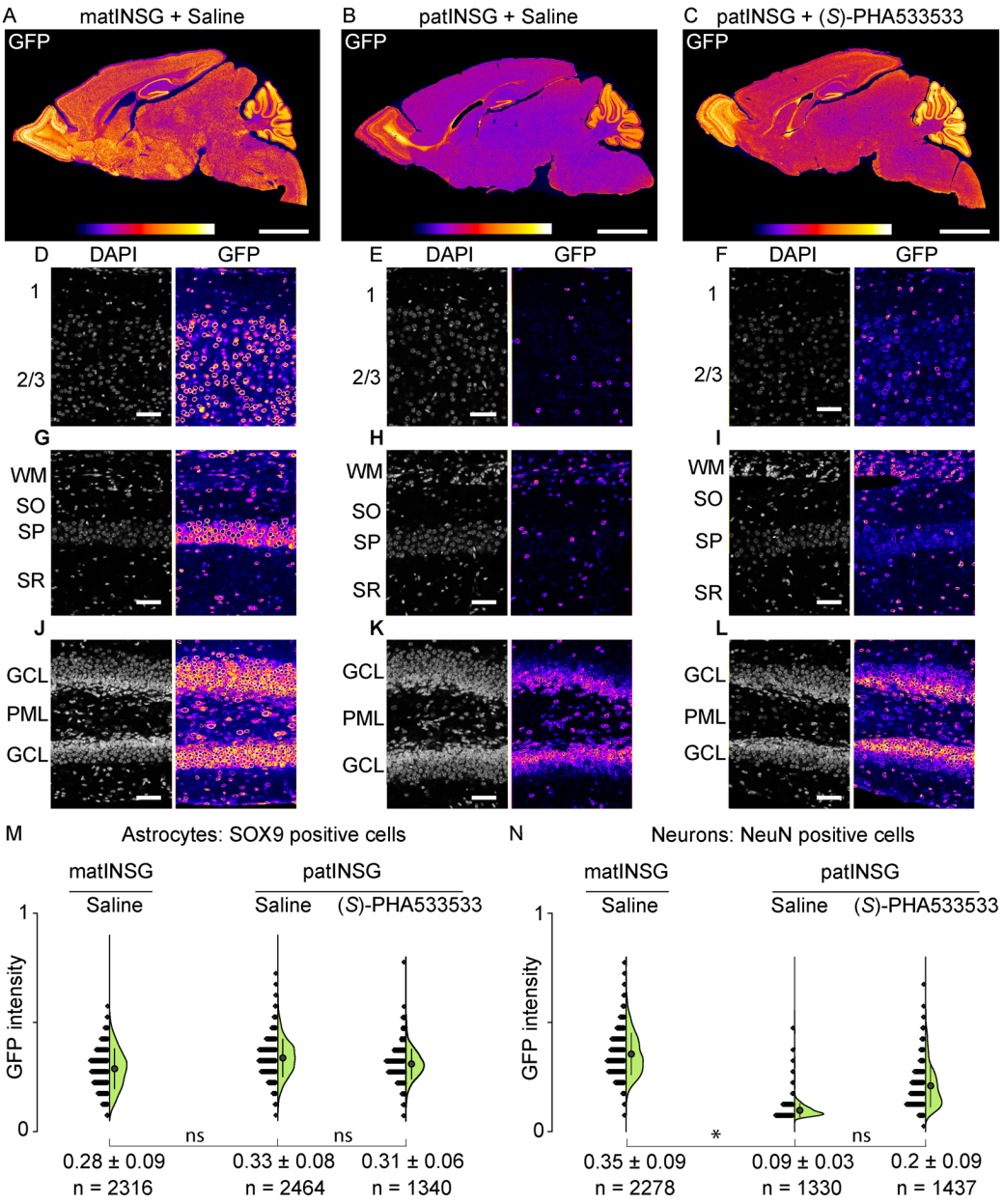

Figure 8. Paternal *Ube3a* unsilencing effect of (*S*)-PHA533533 in mouse brain measured using the Sun1-sfGFP reporter system. matINSG and patINSG mice were treated intraperitoneally at postnatal day 11 (P11) with either saline or (*S*)-PHA533533 (2 mg/kg), and brains were analyzed at P13. UBE3A expression was assessed via GFP immunostaining. (**A**-**C**) Sagittal brain sections visualized using a fire lookup table: (**A**) saline-treated matINSG, (**B**) saline-treated patINSG, (**C**) patINSG treated with (*S*)-PHA533533. (**D-L**) Double staining for GFP (fire lookup table) and DAPI (white). (**D-F**) Layers 1 and 2/3 of the neocortex. (**G-I**) Hippocampal CA1 region highlighting white matter (WM), stratum oriens (SO), stratum pyramidale (SP), and stratum radiatum (SR). (**J-L**) Dentate gyrus, showing granule cell layer (GCL) and polymorphic layer (PML). (**M** and **N**) Violin plots of GFP intensity in CA1 hippocampal cells (N = 3 mice per condition; individual cells shown as n): (**M**) SOX9-positive astrocytes show similar GFP levels across groups. (**N**) NeuN-positive neurons show reduced GFP in saline-treated patINSG versus matINSG, with partial rescue after (*S*)-PHA533533 treatment. Data are

mean ± SD. Statistical analysis by one-way ANOVA with Bonferroni's *post hoc* test. ns = non-significant, *P < 0.05. Scale bars: 2 mm (A-C); 50 μm (D-L).

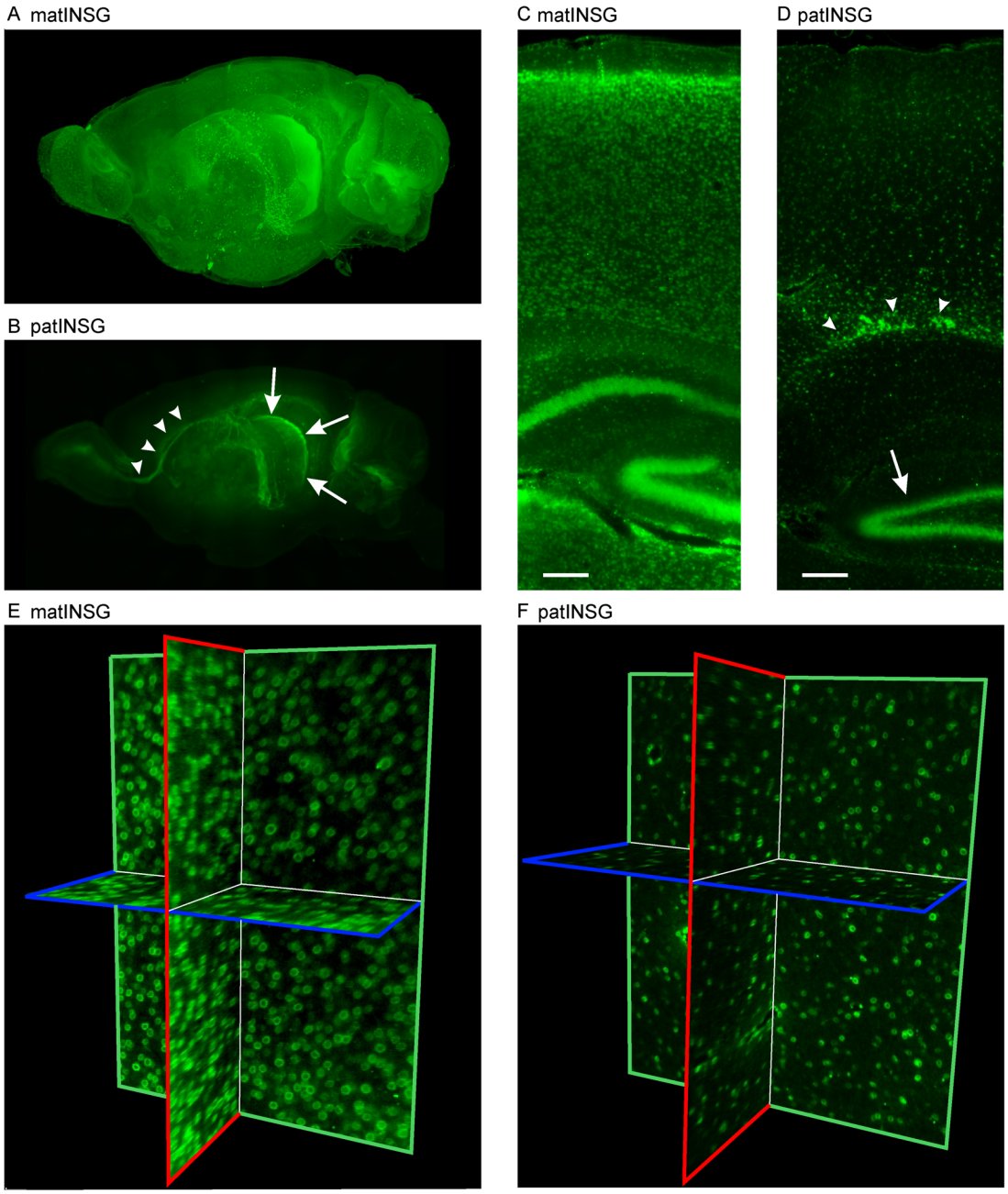

Figure 9. Brain-wide imaging of the Sun1-sfGFP reporter using LSFM. (**A,B**) Maximum intensity projections of left hemispheres from postnatal day 30 (P30) (**A**) matINSG and (**B**) patINSG brains labeled with GFP using iDISCO and visualized with 3D LSFM. The matINSG brain shows robust, widespread GFP expression, whereas patINSG shows lower overall expression, with the strongest labeling in the rostral migratory stream (arrowheads) and dentate gyrus (arrows). (**C** and **D**) Virtual 25 µm slices from (**A**) and **(B)**. (**C**) The matINSG brain shows a strong GFP signal across cortical layers and hippocampus, particularly in the pyramidal cell layer and dentate gyrus. (**D**) In contrast, the patINSG shows markedly reduced labeling, with prominent expression in the subventricular zone (arrowheads) and subgranular zone of the dentate gyrus (arrow). (**E** and **F**) Single light-sheet images in XY, XZ, and YZ planes from the neocortex of (**A)** and (**B**), showing single-cell resolution. In both matINSG and patINSG brains,

individual GFP-positive cells are identifiable, with resolution sufficient to show the nuclear localization of the Sun1-sfGFP reporter. The matINSG neocortex exhibits markedly higher GFP-positive cell density compared to patINSG, with the patINSG neocortex predominantly showing labeling of small nuclei, presumably of glia. Scale bars: 150 μm (C and D).

A

Readout for potency		EC_{50} (μM)	95% CI
Nluc	Norm. RLU	0.42	0.26 – 0.55
GFP	Mean norm. GFP	0.36	0.25 – 0.48
	% GFP⁺ neurons	0.35	0.26 – 0.44

B

Readout for cytotoxicity		CC_{50} (μM)	95% CI
Nluc	Norm. RLU	4.42	4.28 – 4.56
Cell count	Viability (% of DMSO)	4.34	4.00 – 4.68

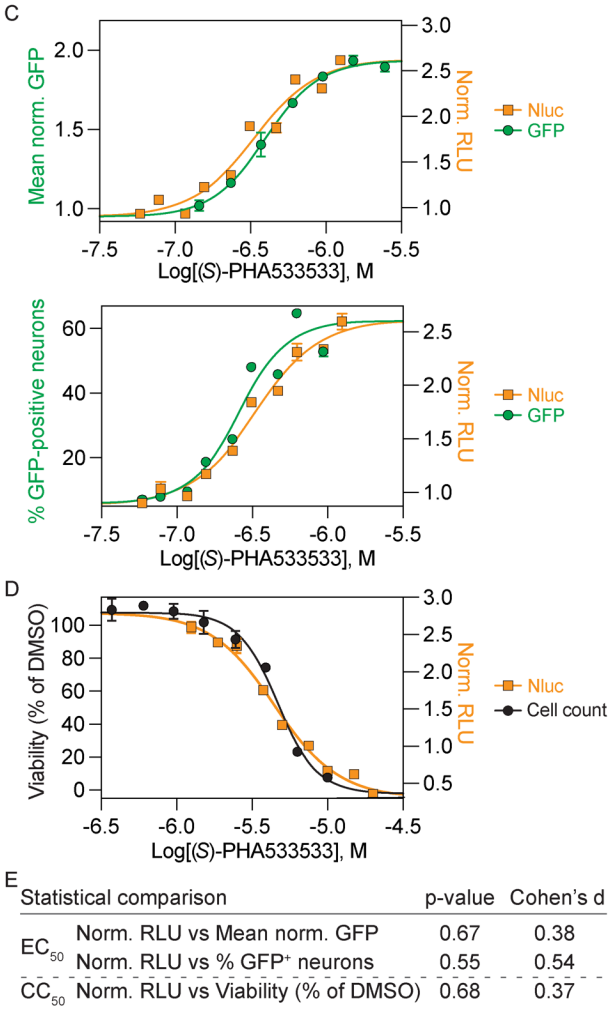

E

Statistical comparison		p-value	Cohen's d
EC_{50}	Norm. RLU vs Mean norm. GFP	0.67	0.38
	Norm. RLU vs % GFP⁺ neurons	0.55	0.54
CC_{50}	Norm. RLU vs Viability (% of DMSO)	0.68	0.37

Figure 10. GFP and Nanoluciferase reporters provide concordant pharmacological readouts for measuring changes in allele-specific *Ube3a* expression in mouse primary neurons from patINSG and matINSG mice. (**A-D**) Pharmacological profiles for paternal *Ube3*a unsilencing in patINSG neurons treated with (*S*)-PHA533533 were assessed using luciferase- and immunofluorescence-based readouts. (A) EC_{50} values from three independent readouts – normalized relative light units (RLU), mean GFP fluorescence, and % GFP-positive neurons – show nearly identical potencies with overlapping 95% confidence intervals (CI). (**B**) CC_{50} values from RLU and viability (% surviving neurons) also show overlapping 95% CI. (C-D) Representative dose-response curves illustrate close agreement between (**C**) Nluc and GFP readouts and (**D**) Nluc and cell count-based cytotoxicity. (**E**) EC_{50} and CC_{50} values between GFP and Nluc assays showed no significant differences. All assays were performed in quadruplicate in three independent experiments (N = 3). Statistical analysis by two-tailed t-tests (E). **P < 0.005, ****P < 0.0001. Norm, normalized.

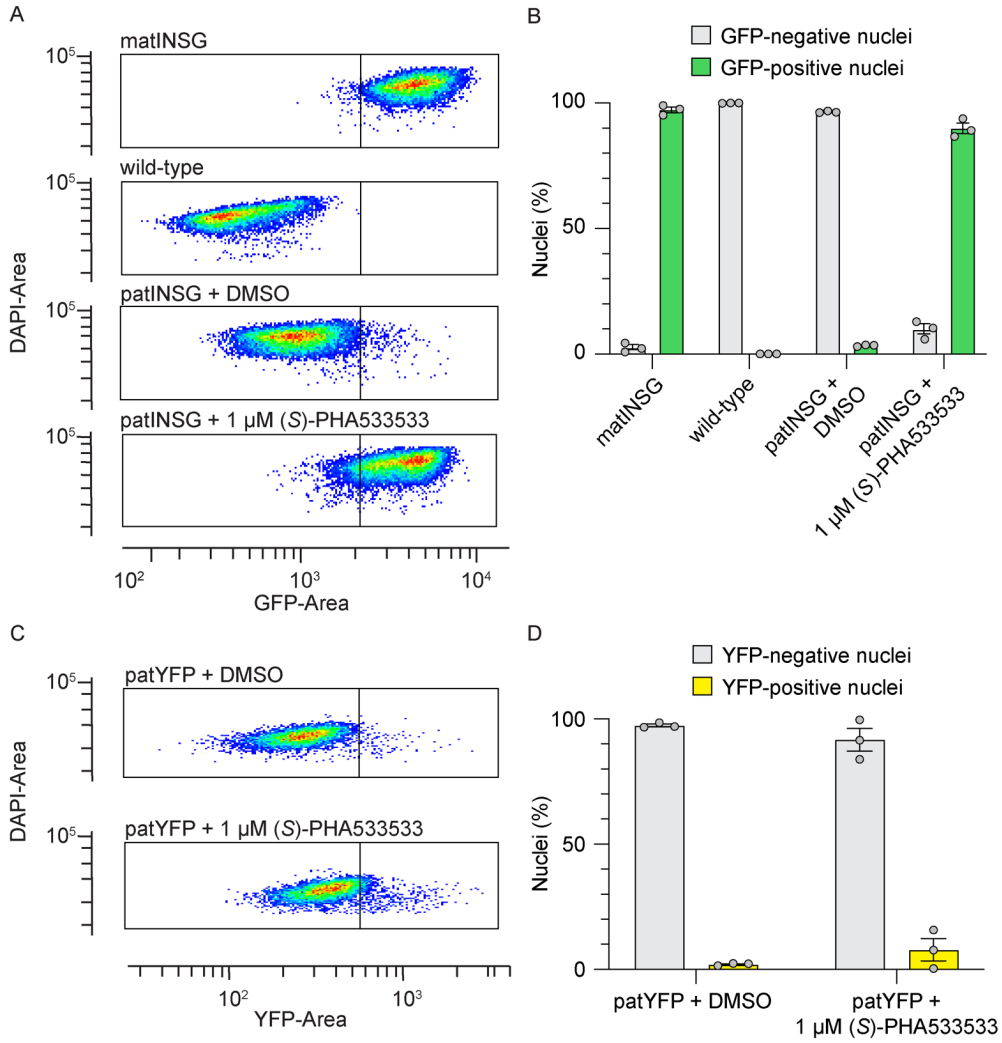

Figure 11. Sun1-GFP reporter enables flow cytometry for detecting paternal *Ube3a* unsilencing. (**A, B**) Flow cytometry was performed to assess the relative fluorescence of GFP/YFP in nuclei isolated from cultured neurons. (**A**) Representative density pseudocolored dot-blots from sorted nuclei pools of cultured neurons derived from matINSG, wild-type, and patINSG mice, with patINSG neurons treated with either DMSO or 1 μM (*S*)-PHA533533 for 72 hours. The boxes indicate the gating boundaries that delineate the GFP-positive and GFP-negative populations. (**B**) Quantification of the percentage of GFP-positive and GFP-negative nuclei across samples. (**C**) Representative density pseudocolored dot-blots from sorted nuclei pools of cultured neurons derived from patYFP mice treated with DMSO or 1 μM (*S*)-PHA533533 for 72 hours. (**D**) Quantification of the percentage of YFP-positive and YFP-negative nuclei across samples. Data are represented as mean ± SEM, where each data point corresponds to an independent well (10,000 nuclei analyzed per well).

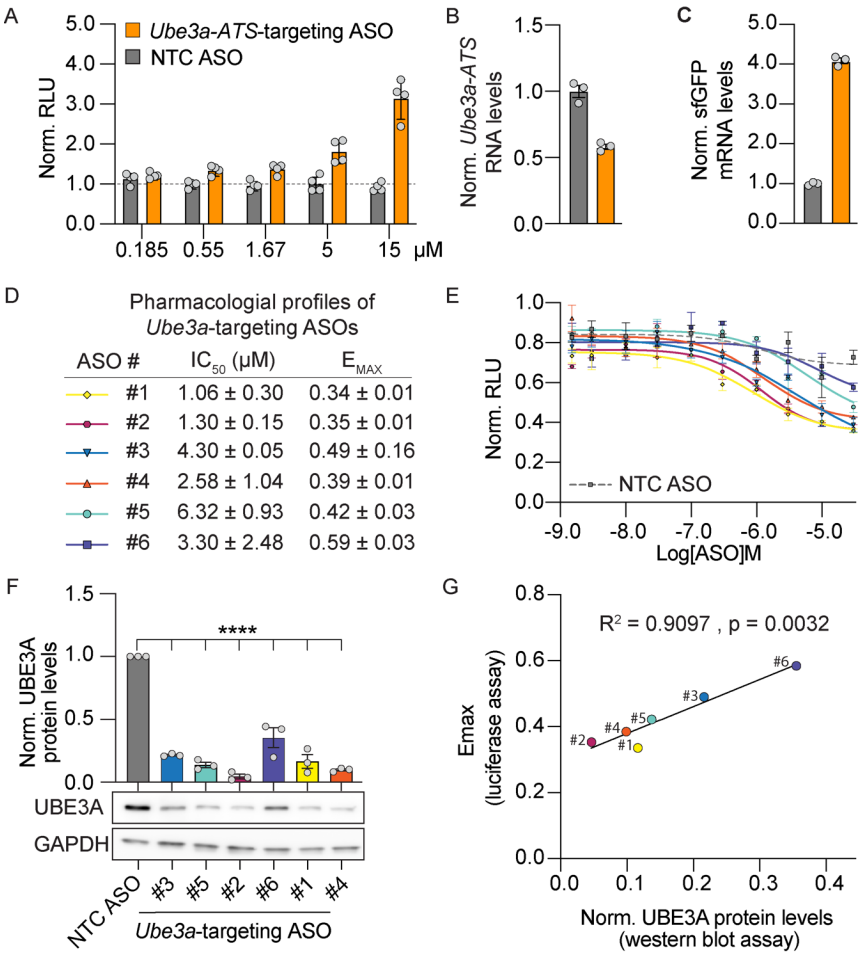

Figure 12. *Ube3a-ATS*-targeting and *Ube3a*-targeting ASOs respectively induce paternal *Ube3a* unsilencing or UBE3A downregulation in INSG neurons. (**A-B**) *Ube3a-ATS*-targeting ASO treatment in patINSG neurons showed dose-dependent paternal *Ube3a* unsilencing compared to non-targeting ASO, measured by (**A**) luciferase assay, and by RT-qPCR at 5 μM ASO for (**B**) *Ube3a-ATS* RNA knockdown and (**C**) sfGFP mRNA upregulation normalized to *Eif4a2* (N = 3-4 wells per group) (**D**) Summary of pharmacological profiles (IC_{50} and E_{MAX}) from luciferase-based *Ube3a* knockdown assays in matINSG neurons by *Ube3a*-targeting ASOs with representative dose-response curves versus non-targeting control (NTC) ASO (N = 3 runs in quadruplicate). (**F**) UBE3A protein levels quantified by western blot in WT neurons treated with 10 μM NTC or *Ube3a*-targeting ASOs (N = 3). (**G**) Correlation between E_{MAX} values from luciferase assay and UBE3A protein levels for *Ube3a*-targeting ASOs, with Pearson's R^2 and p-value indicated. ASO treatments lasted 72 hours. Data are represented as mean ± SEM. Statistical analysis by one-way ANOVA with Bonferroni's *post hoc* (F), and two-tailed t-tests (G). ****P < 0.0001. Norm, normalized.

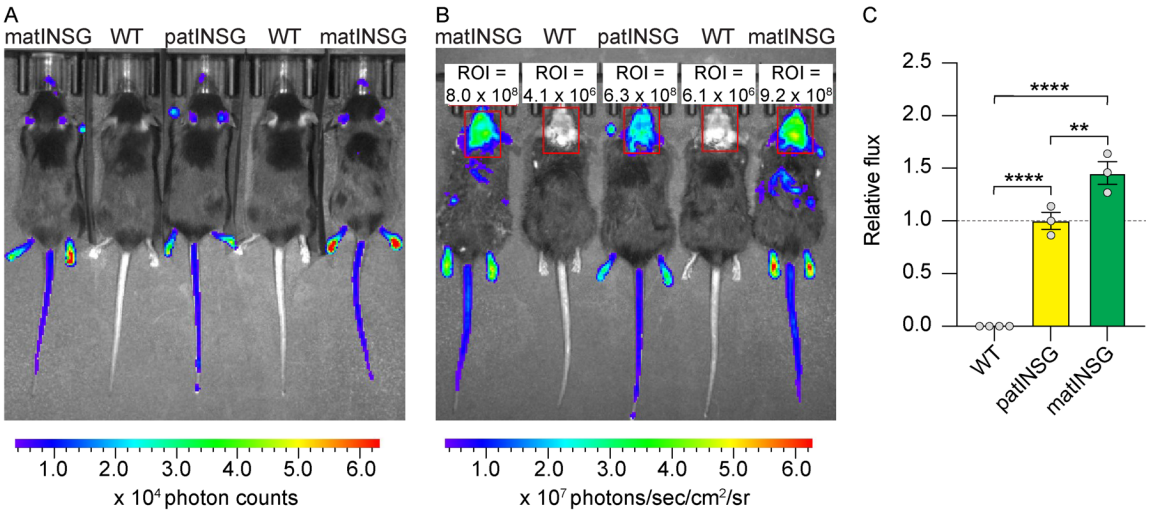

Figure 13. INSG mice enable *in vivo* quantification of UBE3A levels by bioluminescence imaging. (**A**) Representative bioluminescence signal from 12-13-week-old adult female matINSG, patINSG, and WT mice following systemic administration of the Nluc substrate fluorofurimazine. (**B**) Representative images from the same animals after scalp hair removal and repeat substrate administration. (**C**) Quantification of total radiance from matINSG, patINSG, and WT mice, measured as the integrated signal within a standardized head ROI (region of interest) applied uniformly across animals, as indicated. Data were normalized to patINSG mice within the experiment and analyzed by one-way ANOVA with Bonferroni's *post hoc* test. Individual points represent single animals (N = 3-4 per group). Data are shown as mean ± SEM. **P < 0.005, ****P < 0.0001. Photons/sec/cm²/sr – photon per square centimeter per second per steradian.